Corrosion Science 136 (2018) 129–147

Contents lists available at ScienceDirect

Corrosion Science

journal homepage: www.elsevier.com/locate/corsci

Review

A review of uranium corrosion by hydrogen and the formation of uranium hydride

A. Banos*, N.J. Harker, T.B. Scott

University of Bristol, Interface Analysis Centre, School of Physics, HH Wills Physics Laboratory, Tyndall Avenue, Bristol, BS8 1TL, United Kingdom

ARTICLE INFO

Keywords:
B. SEM
B. SIMS
C. Effects of strain
C. Hydrogen permeation
C. Interfaces
C. Pitting corrosion
Uranium hydride
Hydride nucleation
Oxidation behaviour
Surface reactions

ABSTRACT

Uranium hydride (UH_3) is the direct product of the reaction between uranium metal and gaseous hydrogen. In the context of uranium storage, this corrosion reaction is considered deleterious, not just because the structure of the metal may become significantly degraded but also because the resulting hydride is pyrophoric and therefore potentially flammable in air if present in significant quantity. The current review draws from the literature surrounding the uranium-hydrogen system accrued over a 70-year period, providing a comprehensive assessment of what is known about hydride formation, decomposition and oxidation in the context of uranium storage applications

1. Approaches for research on uranium-hydride (UH_3)

Under the correct conditions, uranium and hydrogen readily combine to form a metal hydride (UH_3) in which the metal is transformed from an elemental to trivalent state and the hydrogen becomes chemically entrapped at high elemental density. Historically this reaction between metallic uranium and hydrogen gas (Eq. (1)) has been investigated from two different angles. Firstly, hydrogen corrosion of the metal and secondly, chemical storage of hydrogen, with historically, the former being the prime motivation for research.

$$2U + 3H_2 \leftrightarrow 2UH_3 \quad (1)$$

1.1. Corrosion

When uranium is corroded by hydrogen, the formation of UH_3 results in the physical disintegration of the parent metal. Given that sufficient hydrogen is available, the reaction can be self-propagating [1,2] and occurs at a rate up to four orders of magnitude faster under similar conditions than the rate of uranium oxidation [3]. Such corrosion is deleterious regardless of the storage scenario and the resulting hydride is pyrophoric, which further adds to operational safety issues surrounding corrosion [4]. Accordingly, the prevention of metallic uranium corrosion by hydrogen is a key objective within the nuclear industry worldwide.

1.2. UH_3 potential uses and applications

The hydriding reaction (Eq. (1)) is reversible as the UH_3 decomposes upon heating to uranium metal and H_2 (as discussed in greater detail in Section 5). Thus, uranium can act as an efficient chemical storage material for hydrogen, holding up to almost twice the weight of the gas per unit volume as hydrogen in its liquid form [5]. From a hydrogen storage perspective, it is desirable for the reaction to be optimised in terms of speed, efficacy and repeatability [6,7]. Most recent research has demonstrated uranium as having good long-term performance as a chemical medium for the storage of hydrogen, with the added operational benefits of low hydrogen equilibrium pressure for absorption, low thermal mass and higher thermal conductivity in comparison to other chemical compounds and metals used for storage [8]. Uranium can, therefore, be used as an efficient hydrogen storage material [9] and is often the favoured storage medium for tritium handling facilities [5,10].

These two opposing drivers for research have resulted in a good but not comprehensive understanding of the U + H_2 system. More recently, the reactor research community has added to the list of interested parties for UH_3 research, investigating it as a candidate fuel material for future small modular nuclear reactors (SMRs) [11]. Such SMR concepts harness the effectiveness of H_2 as a neutron moderator with the fact it is evolved from UH_3 at high temperatures. This relationship between temperature and H_2 release creates a feedback loop (charge-discharge

* Corresponding author.
E-mail address: antonis.banos@bristol.ac.uk (A. Banos).

https://doi.org/10.1016/j.corsci.2018.03.002
Received 29 November 2017; Received in revised form 2 March 2018; Accepted 3 March 2018
Available online 13 March 2018

Table 1
The different phases and structural properties of uranium and uranium hydride. U [18,19], UH_3,UD_3 [20–22] and UT_3 [23].

Metal/ compound	Symmetry	Lattice cell parameter (Å)			Density (g/cm^3)
α-UH_3	Cubic	4.160 ± 0.001			11.12
α-UD_3	Cubic	4.150			11.33
α-UT_3	Cubic	4.142 ± 0.002			11.55
β-UH_3	Cubic	6.645			10.92
β-UD_3	Cubic	6.620 ± 0.002			11.11
β-UT_3	Cubic	6.625 ± 0.003			11.29
		a	**b**	**c**	
α-uranium	Orthorhombic	2.85	5.87	4.96	$19.07_{(25\,^{\circ}C)}$
β-uranium	Tetragonal	10.76	/	5.66	$18.17_{(662\,^{\circ}C)}$
γ-uranium	Body centred Cubic	3.52	/	/	$17.94_{(772\,^{\circ}C)}$

cycles) that can allow the reactor to self-regulate its temperature and criticality. Recent work has also shown that due to the kinetic isotope effect between hydrogen and deuterium (D_2), UH_3 shows promise as a material for industrial gas chromatographic separation of hydrogen isotopes [12].

The following sections of this review examine the published literature which describes the physical and chemical properties of UH_3, first focusing on the properties of the material, then the formation reaction, and finally the interaction between UH_3 with its surrounding environment. This understanding is applicable across the spectrum of uses, with greatest importance for safe uranium storage.

2. Fundamental properties

A large density difference exists between the hydride and the precursor metal (Table 1), meaning that UH_3 is a non-protective, autobrecciating reaction product. In such cases the hydride generally appears in a voluminous, finely divided black powder with high surface area [13] and like its particulate metallic counterpart, is highly reactive and pyrophoric under atmospheric conditions [14–16]. However, it is conceivable that this powder could be sintered to produce a near 100% density material [17] or to prepare monolithic hydride by other more advanced methods (e.g. reactive sputtering).

2.1. Crystallographic structure

Two phases of UH_3 are known; α-UH_3 and β-UH_3 (Table 1) [20]. In both phases, each uranium atom is surrounded by 12 equidistant hydrogen atoms at a distance of 2.32 Å [22], as shown in Fig. 1a & b. The lattice parameter for both phases is observed to decrease as a function of molecular weight.

The phase exhibited (or proportion of phases present) is observed to depend on the temperature of formation [24]. The more common phase is β-UH_3 which is formed rapidly, especially at high temperature [25–27]. A small number of studies have investigated the relationship between hydride phase and formation temperature (See Table 2). The proportion of α-UH_3 phase forming is reported to increase with decreasing reaction temperature, and given a sufficiently low reaction temperature, a pure α-UH_3 phase may be formed; however, at very low temperatures and ordinary pressures, the rate of hydride formation would be small and a pure sample of bulk α-UH_3 has yet to be formed. Therefore β-UH_3 is regarded as the 'default' hydride reaction product, and the expected phase for most reaction conditions explored in the literature.

2.1.1. α-UH_3

The more compact of the two hydride phases, α-UH_3 has been observed to possess a cubic lattice (Pm3n) with 2 uranium atoms per unit cell, of dimension 6.160 ± 0.001 Å (Fig. 1a) [20]. Results from

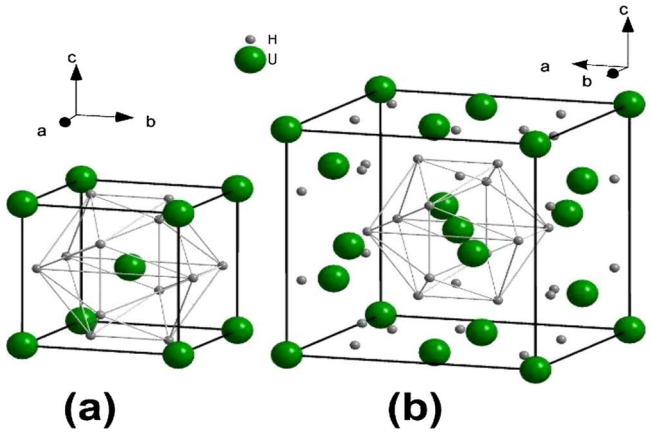

Fig. 1. Crystal structure of (a) α-UH_3 and (b) β-UH_3 drown using Diamond (version 2.1c) software. The small and large spheres stand for hydrogen and uranium atoms, respectively. For α-UH_3 the 12 nearest hydrogen atoms are shown around the U (½,½,½) atom, occupying the H: ± (1/4,0,1/2) (1/2,1/4,0), ± (0,1/2,1/4). For β-UH_3 the 2 UI ions sit on the bcc lattice, whilst the 6 UII atoms make up the rest of the structure. The hydrogen atoms around the UII lie on: ± (0,u, ± 2u), ± (1/2, ± 2u,1/2+u) where u = 0:155. All UI and UII distances are the same. Figure reproduced from reference [102].

Table 2
The proportion of α:β-UH_3 formed over a range of temperatures.

Temperature (°C)	a:β-UH_3	Reference
−80	1:0	[20,25]
Room temperature	1:1.5	[20,25]
125	1:5.7	[20]
200	0:1	[25–27]

atomistic modelling have suggested that α-UH_3 is isomorphous with α-U but not β-UH_3, allowing α-UH_3 to form via spinodal decomposition in a hydrogen saturated metal to then act as nucleation sites for subsequent β-UH_3 formation [28].

2.1.2. β-UH_3

Like with the α-phase, β-UH_3 has been observed to possess a primitive cubic lattice (Pm3n) with 8 uranium atoms per unit cell, of dimension 6.643 ± 0.001 Å for UH_3 and 6.627 ± 0.001 Å for UD_3, with the atomic position of the hydrogen atoms as y = 0.155 ± 0.016 Å and z = 0.303 ± 0.002 Å and deuterium y = 0.1556 ± 0.006 Å and z = 0.3041 ± 0.006 Å [21]. By simple calculation using the data from Table 1, it can be seen that α-UH_3 holds ≈ 1.105 times as much H_2 as β-UH_3 per unit volume. Also, according to theoretical data, α-UH_3 contracts with applied pressure by 0.25 A^3/GPa for low-pressure regimes [29] while for β-UH_3 and for applied pressures up to 29 GPa a more modest 13% contraction may be observed [30].

The activation energy for the diffusion of hydrogen or deuterium into, α-UH_3 and β-UH_3 were found to be 35.1 ± 3.8 kJ mol^{-1} and 37.2 ± 3.8 kJ mol^{-1} respectively, for temperatures > 370 K [21]. Below room temperature, hydrogen readily exchanges between surface adsorbed H_2 and the UH_3 [31]. The rate of exchange between gas and solid, for environments of 70–700 kPa H_2 between 25–400 °C, has been found to be controlled by the rate of hydrogen transport within ~0.7 μm diameter hydride particles [12].

At 100 °C, α-UH_3 has been recorded as co-existing in a stable state with the β-phase but is totally converted to β-UH_3 upon heating to 250 °C [20,26]. This is accompanied by a 1.7% volume expansion due to the density difference. The opposite transformation was not witnessed when the conditions were reversed [20,27]. Thus, the hydriding temperature and any thermal excursions that occur during confinement directly influence the form of the hydrogen corrosion product that persists. The heat of formation of UH_3 and UD_3 measured at 25 °C (i.e. a

combination of α-UH_3 [20] and β-UH_3) have been recorded as $-127.0\,kJ\,mol^{-1}$ and $-129.8\,kJ\,mol^{-1}$ respectively, [25] and in both isotopic forms the formation is notably exothermic. Work looking at the H_2 exchange with UD_3 found the free energy difference between the two phases to be small [31], and that the H_2 in UH_3 has been observed to readily exchange with D_2 at, and below, room temperature [12].

2.2. UH_3 morphology

Due to the pyrophoric nature of UH_3 when exposed to the air, direct characterisation is challenging, especially when a high surface area and mass of hydride exists. Safe handling within non-specialist laboratories is only possible when small masses of material are used i.e. isolated hydride spots on a metal surface. Accordingly, it is of significant operational interest to be able to predict the morphology, particle size and surface area of uranium hydride that could form in any given storage environment.

To produce metal powders of high surface area for subsequent oxidation corrosion experiments [13,32–34] hydriding-dehydriding cycles are used as a method for disintegrating precursor metal blocks. If this cycle is repeated numerous times, the mean particle size of the material is found to approach a constant value (Fig. 2) [34]. This is reflected in the reaction kinetics as shown in Fig. 3 and it has been observed that after six cycles, the reaction kinetics remain the same providing the reaction conditions remain the same [7]. In the first couple of cycles, the hydriding step has been reported to yield a U/H ratio which is less than three indicating the reaction may be initially non-stoichiometric or incomplete but normalizes after the third cycle [35].

Fig. 4 shows secondary electron (SE) images of a uranium powder that has been prepared by six hydriding-dehydriding cycles followed by a period of controlled oxidation (in H_2O vapour and O_2 gas), after which the material was allowed to stabilize in air before being loaded into a focused ion beam (FIB) instrument for imaging [13]. The reaction product is angular in appearance with the individual particles appearing lozenge-shaped, or as elongate cuboids with a roughened exterior. The size ranges from 15 ± 10 μm × 5 ± 2 μm. This reaction product matches the description given by other investigators for uranium subjected to 50 hydride-dehydride cycles, followed by several hours of air exposure. They describe the final product as cylindrical or 'wire' like, possessing branching thread-like extensions 0.01–1 μm thick [7].

Imaging at higher magnification identified the oxide grown from the particles as having a stacked plate-like character (Fig. 5). These appear to fracture creating an oxide spall ranging from micron to sub-micron in size. Fig. 6 shows a cross-section through a post-reaction uranium particulate. The morphology of the surface oxide is variable, reflecting the underlying particulate shape. The thickness is uneven reflecting the ease with which the oxide can spall due to the lack of lateral retention. Despite the uneven appearance, there does appear to be a consistent base thickness of oxide surrounding the particle. This suggests corrosion of uranium produces a fine material which could subsequently be easily disseminated if released.

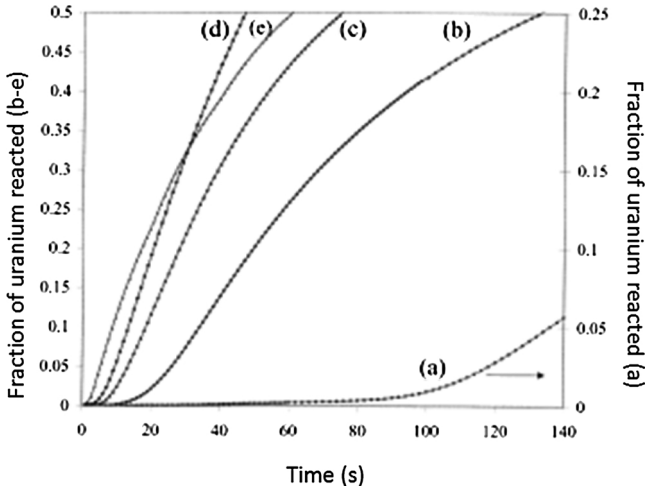

Fig. 3. A graph displaying proportion of UH_3 formed from uranium metal as a function of time for samples that have experienced a number of prior hydriding cycles, (a) 1, (b) 2, (c) 4, (d) 6 and (e) 50. Hydriding was performed at 370 °C, 62.5 kPa H_2. Graph adapted from [7] and reproduced from reference [102].

The average surface area of the material shown in Figs. 4–6 along with similarly prepared samples from other studies performed by the authors [13] were determined via Brunauer–Emmett–Teller (BET) analysis using nitrogen gas and gave a result of = $0.72\,m^2\,g^{-1}$, with a standard deviation = $0.45\,m^2\,g^{-1}$. This compares well with the spread of other data available in the literature for hydrided and dehydrided uranium metal powder where recorded results ranged from 0.33 to $3.62\,m^2\,g^{-1}$ [14,34,36–38], implying that the result for both hydrided or dehydrided metal is very similar. Indeed, due to the volatility of the reaction product, few studies have achieved a direct measurement of hydride without some degree of oxidation. Results from assorted uranium corrosion products (oxidised hydride, fuel, oxidised metal) are far more varied, ranging from 0.5 to $1.04\,m^2\,g^{-1}$ [14,39]; 2–$12.9\,m^2\,g^{-1}$ [32,34,40] even as high as $30\,m^2\,g^{-1}$[38], suggesting different levels of oxide spallation and break-up for the recorded surface area values.

For the use of hydride as a possible SMR fuel material, this research

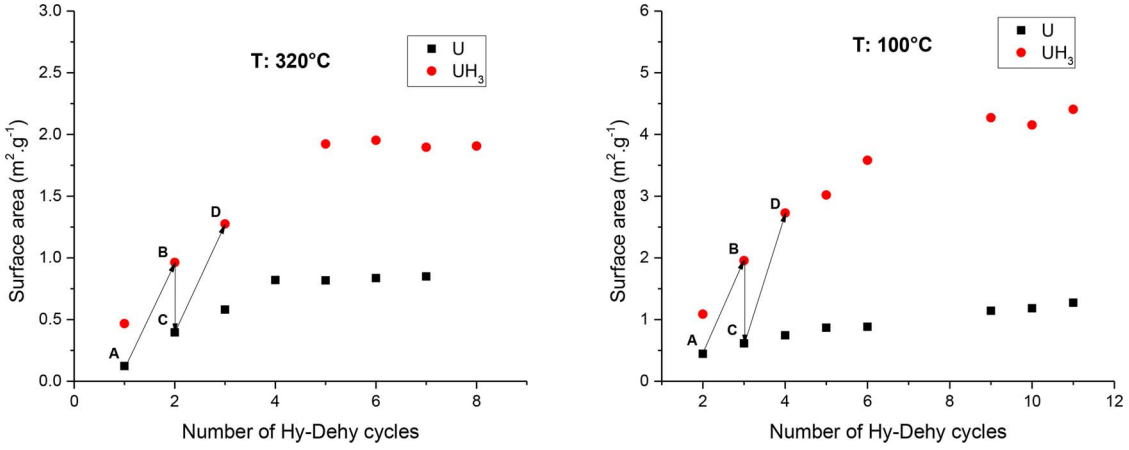

Fig. 2. Showing the change in particle size for uranium and uranium hydride (UH_3) powder after successive hydriding-dehydriding sessions at (a) 100 °C and (b) 320 °C. The arrows signify the sequence of the reactions with A → B → C indicating the Hydriding → Dehydriding → Hydriding step. Graph adapted from [39] and reproduced from reference [102].

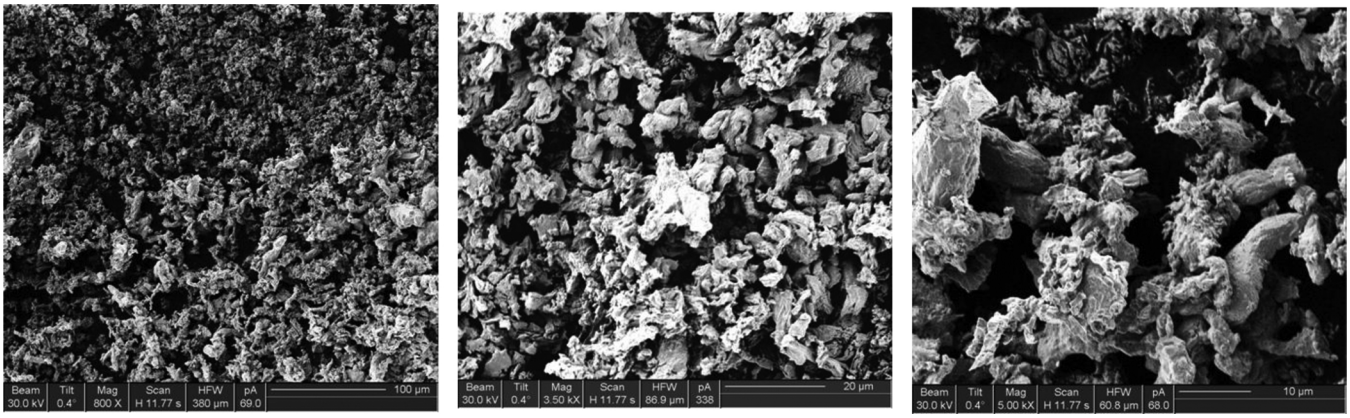

Fig. 4. Secondary electron (SE) images of increasing magnification for a uranium powder prepared via six hydriding-dehydriding cycles and passivated via controlled H_2O + O_2 exposure and stabilization in air. Graph adapted from [13] and reproduced from reference [102].

is useful in predicting the through life particle size and surface area of over multiple cycles of hydrogenation and dehydrogenation.

3. The U + H_2 reaction

The initial development of hydride on lightly oxidised metallic surfaces is, for many binary metal-hydrogen systems, characterised by the appearance of growing hydride "spots" on the metallic surface [1,2,41–45]. For a hydride spot to nucleate the flux of hydrogen to the metal surface must exceed that which is diffusing into the bulk metal to allow saturation to occur [3,46]. As both increase exponentially with temperature, the nucleation rate may be slowed if the gas pressure is inadequate [46]. The number density of the hydride spots is finite and dependent on the solubility of H_2 and the microstructure of the metal [42]. Provided that there is sufficient hydrogen to allow continued reaction, the nucleation centres tend to grow radially and eventually merge to form a continuous hydride layer at the metal surface. This then thickens by the so-called 'shrinking core' morphology to ultimately consume the whole sample [47,48]. For the bulk hydriding stage and over a wide range of temperatures (25–500 °C) the activation energies (E_α's) have been given a range from 23.2–39 kJ mol^{-1} [7,28,41,49–54]. From the data four stages have been associated with the uranium-hydrogen reaction [55]:

1. **An induction period**. Under normal conditions, the metal surface is covered with a surface passivation layer (SPL) of oxides, hydroxides, oxycarbides and water [46] which acts as a barrier to hydrogen diffusion [56] and also removes dissociation sites [57].
2. **Nucleation and growth of discrete UH3 sites**. This occurs at the point or points where the SPL has failed. Initial hydrogen attack is termed as 'nucleation'. This expression is broadly accepted due to the almost hemispherical way that the sites spread on the metal surface [1]; however, UH_3 has also been observed in strip-type [58] or filiform-like morphologies [59].
3. **Bulk reaction**. This occurs when the discrete reaction locations coalesce to form a homogeneous reaction front. The transition may be delayed or even not observed depending on the gas purity [43], temperature regime [60] and geometry of the reacting sample [42].
4. **Total conversion of bulk metal to UH_3**. The progression of the hydride reaction front into the metal continues until total consumption occurs, and the reaction slows and eventually ceases.

These stages are highlighted in Fig. 7 which shows the idealised pressure decrease of hydrogen over time due to reaction with a uranium metal powder at 320 °C. The duration of these stages depends on the form of the uranium metal, (i.e. powder or a solid) as kinetics differ depending on the surface area to volume ratio [46,51]. The size and shape of the metal not only affect the reactive surface area [61], but also affect the heat release [62], accelerating temperatures away from isothermal conditions [63], and reducing or even removing the induction time [61]. Hence, the formation of UH_3 would appear to be a simple process. However, in practice, the situation is much more complex. Therefore, it is the factors controlling the induction period and initial nucleation and growth site formation which ultimately determine the fate of uranium metal in a hydrogen environment. In the early hydriding stage, the reaction is considered to be controlled by two

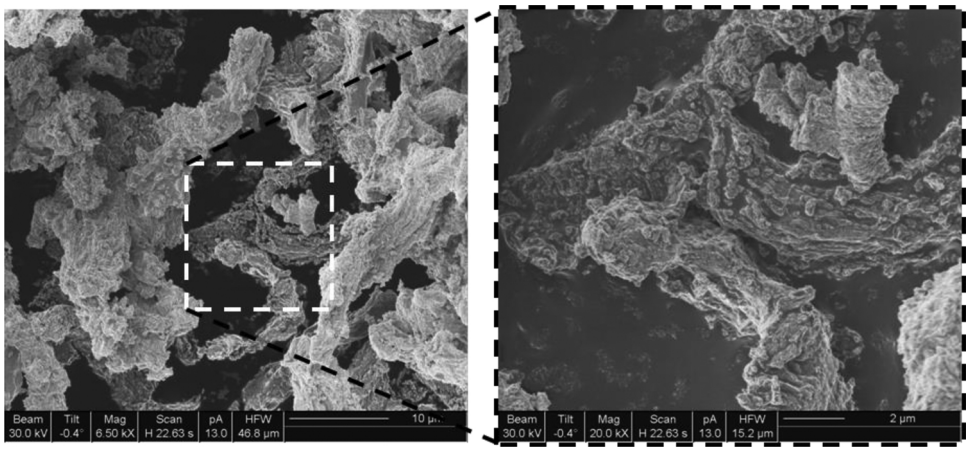

Fig. 5. Two secondary electron (SE) images displaying oxidised uranium particles, showing the laminate oxide grown on their surface. Graph adapted from [13] and reproduced from reference [102].

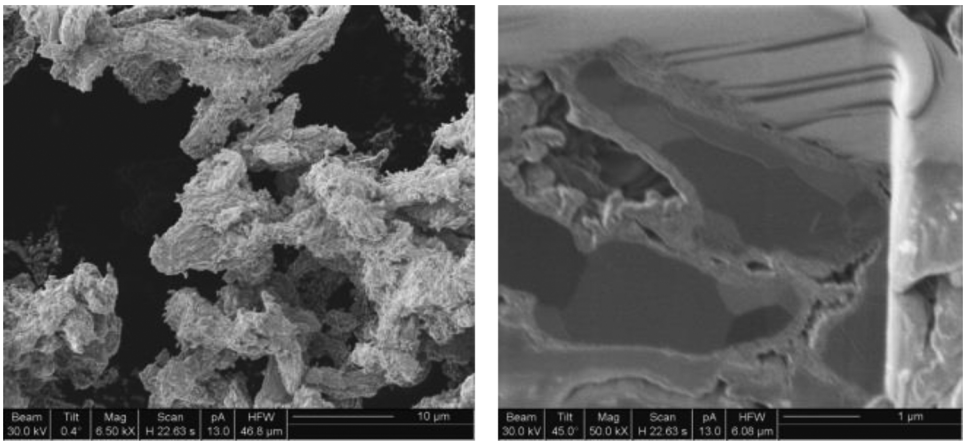

Fig. 6. Focused ion beam (FIB) and secondary electron (SE) images showing on (a) a uranium particle before cross-sectioning, and (b) a high magnification image of the cut face. Note the recrystallised grain structure of the metal particle shown in (b). Graph adapted from [13] and reproduced from reference [102].

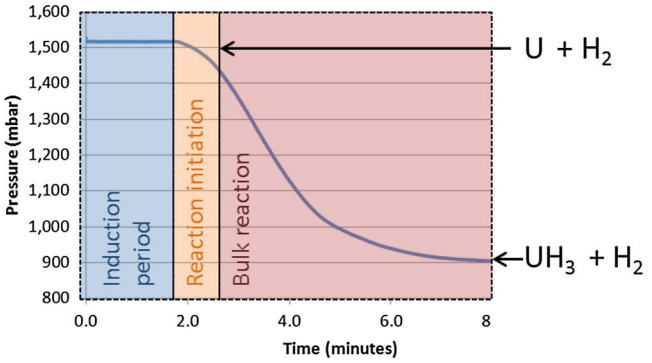

Fig. 7. A graph showing a U + H_2 reaction performed at 320 °C on a 0.19 g uranium sample. The reaction was performed in a fixed volume of H_2 gas, hence the pressure decrease with time. Graph adapted from [13] and reproduced from reference [102].

main factors: the environmental conditions surrounding the metal (temperature, hydrogen purity and pressure) [24,64,65] and the characteristics of the metal surface and its oxide [66], which is now be explored further.

3.1. The induction period

The generally accepted view is that hydride nucleation and the subsequent growth of nucleated material is preceded by a period in which hydrogen penetrates the SPL [42,55,56]. Previous work has shown that the duration of this 'induction' period is dependent on several factors, namely, oxide thickness, oxide heterogeneity, degree of surface hydroxylation, abundances of impurity phases in the metal, such as carbides and the purity of the H_2 gas.

When hydrogen permeates the oxide layer, it begins to build-up at the oxide-metal interface. The mechanism for H_2 permeation and diffusion has not yet been clarified and could vary depending on the oxide stoichiometry. When the concentration of hydrogen in the metal at this interface exceeds the hydride solubility limit (a temperature-dependent parameter) the gas-solid hydriding reaction takes place. Overall, the hydrogen concentration in the metal near the oxide-metal interface is governed by the net difference in the abundance of incoming H atoms passing the oxide-metal boundary, relative to the abundance of the outgoing H atoms diffusing into the bulk of the metal.

Thus, for oxide-coated uranium, the physical build-up of hydrogen at the oxide-metal interface prior to the hydride forming reaction can be described by the following sequence of elementary steps [67] (highlighted in Fig. 8):

1. **Surface Sorption:** Physisorption of H_2 at the oxide surface, followed by either diffusion or dissociative chemisorption of two H atoms and/or ions.
2. **Permeation:** Surface to subsurface penetration and diffusion of hydrogen through the oxide layer coating the uranium metal. This may occur as; molecular H_2 or via a dissociative chemisorption step to atomic or ionic H.
3. **Concentration:** Build-up of H atoms at the oxide-metal interface, towards the hydride solubility limit leading to reaction.

The model of Cohen et al. [68], defined the first two steps of this process (surface sorption and permeation) using a combination of diffusion- and surface-related properties. The sorption step of the hydriding process was described as a function of two temperature-dependent surface sorption related parameters of the oxide film, namely its H_2 surface sticking property and desorption rate constant. The permeation step was described as a function of two diffusion related parameters of the oxide film: its thickness and its diffusion rate constant [68]. The induction period and the initiation of hydride nucleation sites are interlinked, as the former relates to the ease with which H_2 can access the metal, and the latter highlights the first point of attack on the metal surface. The factors controlling these processes (induction period, initiation of hydride sites and hydride location) are discussed below.

3.1.1. Hydrogen purity

If the H_2 gas to which the uranium is exposed is contaminated with impurity gases such as O_2, H_2O or air, the observed induction period is increased and the reaction rate suppressed [43,69]. This is ascribed to either enhancement of the SPL by further oxidation or leading to competition for surface sorption sites with the impurity gases [41,46]. Impurities can also potentially saturate the oxide, blocking diffusion pathways [70]. If the impurity is oxygen or water, there is also a competing anion for reaction with the uranium [37]. Many experimental failures in reproducing the uranium-hydrogen reaction are a result of contamination, usually the result of ingress of atmospheric gas (O_2 contamination).

3.1.2. The oxide

The primary natural barrier that uranium has against its external environment is its oxide layer which covers the metal surface. The strong affinity of uranium for oxygen is widely established [71–74] and under ambient conditions, any freshly polished or cleaned uranium surface would be expected to have an immediately formed and initially thin coating of uranium oxide, formed by reaction of the metal with the ambient (or sometimes controlled) atmosphere. The oxide phases of uranium between UO_2-UO_3 are the principal products of uranium metal

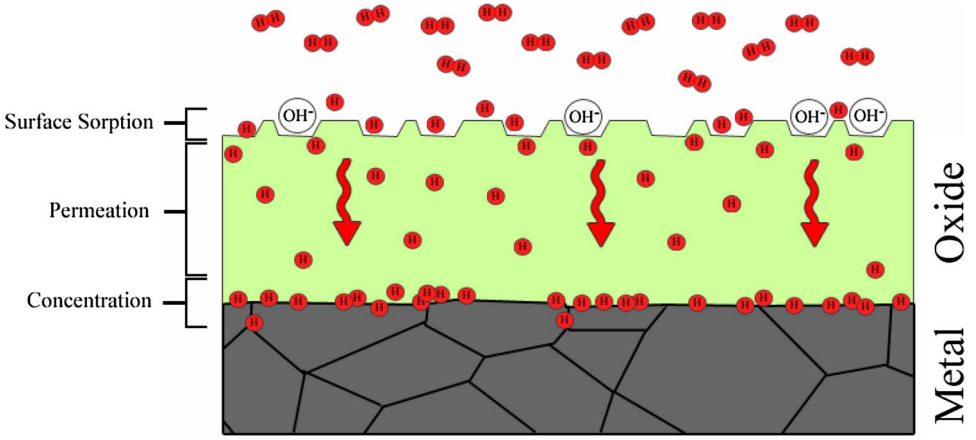

Fig. 8. Diagrammatic representation of the three-step sequence for the physical build-up of hydrogen at the oxide-metal interface of uranium prior to the occurrence of a hydride forming reaction. Graph reproduced from reference [102].

corrosion and have been studied in detail [71–79]. Once formed, the oxide forms a passive layer decelerating further corrosion, and so act as an additional barrier to the onset of hydride formation. The solubility of H_2 in UO_2 as experimentally determined by Wheeler [80] is reported as 0.03–0.4 $\mu g(H_2)/g(UO_2)$ depending on the defect structure of the single crystal [80]. Sherman and Olander [81] reported notably lower values up to three to four orders of magnitude smaller than those of Wheeler [81]. Parameters such as oxide stoichiometry and single- or poly-crystallinity were found to notably affect the solubility of H_2 [81], though the volume of research on this matter is limited and arguably requires greater attention.

The induction time to UH_3 formation (after initial exposure to H_2) is recognised to depend on the reaction temperature and H_2 pressure [55]. However, it is also found to increase with increasing oxide thickness [70] suggesting a control exerted by the increasing transport path-length; though only up to a thickness of ~50 nm [56] after which the effect is lost, attributed to a loss of coherence of the oxide, i.e. cracking and spallation. For controlled dry oxidation the passivating properties of the oxide layer were found to be effective up to a thickness of ~200 nm [56]. Interestingly, it has been found that vacuum annealing heat treatments prior to hydriding reaction greatly enhance UH_3 initiation by reducing the preceding induction period and increasing nucleation rates [52,82,83]. This effect is not unique to the uranium-hydrogen system [84,85] and has been attributed to modifications of the oxide layer induced by heating from:

i. Desorption of physisorbed and chemisorbed water (part of the SPL), which leaves the outermost surface of the passive oxide layer more active to H_2 uptake − increasing the surface sticking property [24,86].
ii. Slight changes in the stoichiometry of the oxide induced by heating (i.e. the oxygen to metal ratio) resulting in an increased diffusivity [87]. Recent studies by Knowles [88] also showed that partial oxide transformation into an UO_xC_y sub-layer may be observed at the metal-oxide interface as part of high temperature (> 200 °C) thermal annealing. These phase modifications could result in enhanced mobility of H_2 through the oxide lattice [88].

Correspondingly, this thermal treatment is found to significantly reduce or even remove the reaction induction time [70]. It is notable that for hydrogen storage applications, hydride that has undergone decomposition in an oxygen-free environment has little or no SPL, and so it is highly reactive (sometimes termed “activated”) with oxidising species or re-hydrogenation.

The hydride’s subsequent growth becomes independent of these oxide limiting parameters only after the oxide over-layer becomes ruptured [43]. Evidence suggests that the induction period prior to the hydriding reaction is controlled by variations in the above diffusion and surface related properties of the oxide.

3.2. Location of nucleation sites

The initial development of hydrides on massive metallic surfaces is observed to occur in isolated zones or ‘spots’ [1,2,41–45], indicating that certain surface areas are more favourable for the onset of hydride-forming reactions [56,59,89]. These nucleation sites lie at the metal-oxide interface and not in the metal subsurface [90].

As previously stated, the precipitation of a hydride phase resulting from a gas-solid reaction only occurs when the local concentration of H_2 in the metal exceeds the solubility limit. During a hydriding experiment, it follows that the first hydride spots to form do so in areas where the SPL is weakest or the metal most susceptible, leading to hydrogen build up and initial nucleation of the hydride phase. For example, in a ‘natural’ uranium-hydrogen system the composition and thickness of the oxide layer may differ at locations across the surface due to defects, cracks and topographic variations. Owing to the inhomogeneity of this surface oxide layer, the physisorption of hydrogen onto the oxide and its subsequent permeation through this layer to the oxide-metal interface varies across the surface, providing ‘active’ zones where H_2 reaches the critical concentration faster to nucleate first [91]. These regions could potentially be identified prior to hydriding experiments.

3.2.1. Hydride growth types

The picture is further complicated by observations that the character of the hydride may differ depending on its rate of growth or due to the characteristics of its nucleation site on the metal surface [2,66]. Four types of hydride nucleation families have been identified [2], tending to be characterised by either a high nucleation rate with a low growth velocity or vice versa [46]:

i. Sub-micron sized blisters with a high surface distribution density tend to be located on scratches.
ii. 1–10 μm blisters formed below the oxide layer at point defect sites on the metal surface. The oxide acts to confine and slow the UH_3 growth [92,93].
iii. Hydride nucleation around carbide inclusions at the metal surface.
iv. Rapid growth at oxide discontinuities or features of the metal surface such as twins or grain boundaries.

It has been observed that prior to the development of hydride growth spots, nucleation and growth of sub-micron size hydride spots occurs. The growth of these nuclei proceeds below the oxidation layer,

and occasionally their volume expansion is insufficient to rupture the overlying oxide layer. Hence, a substantial compression field can be generated, which increases with the size of the grown nucleus, resulting in slow and decelerating growth rates of the nuclei. In fact, if no rupture of the oxidation layer occurs, the growth of the hydride nuclei finally halt, attaining a certain critical size range (< 3–4 μm) typical of a 'small' family precipitate [94].

If the oxide over-layer becomes ruptured by the growing hydride nucleus, the compression field is relieved, and the initiation of more rapid hydride growth occurs, as it becomes independent of the confining oxide. In this case, a hydride growth typical of a 'large' family precipitate develops. Thus, it is assumed that the formation of a 'large' family hydride growth site is related to a special location where the rupture of the oxidation layer is easier, e.g. a micro-crack, along with an oxide-carbide interface, or an area where the oxide is thinned. However, weaknesses in the metal lattice which provide nucleation sites for hydride formation cannot be separated from the structural effect these defects have on the oxide layer that has formed overlying these sites [58,95]. Metal surface defects can propagate through the oxide, i.e. susceptible areas tend to enhance their own weakness to hydrogen attack. The main features which have been identified are now described.

3.2.2. Surface damage

Scratches or any other extrinsic damaging to the oxide or SPL provide a direct route for H_2 to reach the metal surface and are well-established loci for hydride nucleation [2,96,97], as highlighted in Fig. 9. The sample shown in Fig. 9 was polished (~20 nm surface roughness) and annealed at 550 °C for 16 h under UHV before being exposed to air for five minutes to thicken the surface oxide. The sample was then scratched with a pair of stainless steel tweezers in an Ar-filled glove box before being reacted at 250 °C with a D_2 gas pressure of 500 mbar. The reaction was halted after a 5-mbar pressure drop was observed and the sample transferred to the FIB then secondary ion mass spectrometry (SIMS) instrument for analysis. FIB imaging (Fig. 10) revealed a significant incidence of corrosion along the length of the surface scratch, which SIMS positive ion mapping (Fig. 10) revealed to be UD_3. Ion clusters associated with deuteride growths (UD^+, UD_2^+, UOD^+, UO_2D^+ and $UO_2D_2^+$) could be clearly resolved relative to the U^+, UO^+ and UO_2^+ ion clusters more typically associated with the surface uranium oxide.

3.2.3. Surface inclusions

Inclusions are not coherently covered by the surface oxide, and so can provide gaps or physical disruptions in the metal oxide, providing a passage for hydrogen along the inclusion-oxide interface (Figs. 11 and 12). Such pathways are considered to enhance transit through the bulk oxide [1,58,98]. Therefore inclusions in uranium have been found to act as preferable nucleation sites for hydrogen attack [1,2,58,59,95] though this has not been observed by all studies [99,100] as these sites can be passivated by electropolishing [98,101]. Hydrides around these regions exhibit a high growth velocity breaching the oxide surface and moving deep into the metal while joining up to form large pits [1,96].

Nucleation at these sites may be influenced further by the geometry of the inclusion with respect to the metal surface and by residual stresses in the surrounding metal allowing a localised concentration of H_2 in the metal. The low activation energy at the margins of these sites allows easy access of hydrogen to these regions. Exploratory work has been carried out using electron back-scattered diffraction (EBSD) to look for crystallographic distortion as an indication of residual strain in the metal lattice [13] (Fig. 13). Whilst this work has yet to be built upon it provides tantalizing evidence to show that elevated levels of crystallographic distortion can be identified surrounding inclusion sites which can be related to the differing thermal expansion coefficients of the uranium metal and uranium carbide.

3.2.4. Grain boundaries

Grain boundaries are well-established as preferential sites for hydride nucleation [42,59,65,90,96,99,101,102], especially in higher purity metals where inclusion particle number density is low. Recent work in our lab [101], employed EBSD to statistically analyse hydride growth location on natural Magnox uranium. The analysis has shown that more than 90% of the hydride growth sites were directly related to grain and twin boundaries (Fig. 14a & b). Grain boundaries (including sub-grains and twins) are believed to have a greater diffusion coefficient than the bulk grain and, so, provide a route into the metal subsurface, allowing concentration of hydrogen within the metal [59]. The angle of incidence of the grain boundary with respect to the metal surface is also believed to alter its favourability as a site for hydride formation [65]. Boundaries which intersect the metal surface at an acute angle are thought to be more susceptible to reaction as a larger area of the grain boundary region is exposed and the wedge tip of the grain is geometrically favoured for most rapid hydrogen accumulation, as shown in the schematic in Fig. 15 [65]. In addition, it has been observed that the rate of metal oxidation varies with crystal orientation in the early stages of oxidation [95]. This results in a structural discontinuity in the oxide over grain boundaries that may enhance the ingress of hydrogen to these locations [95,101]. Fig. 16 provides a schematic to explain this process with y_A, y_B and y_C representing the thickness of the oxide for grains A, B and C, as a function of oxidation time. At t_1, oxidation rates between the grains sharing a low misorientation angle boundary (LMA) are comparable ($y_A \approx y_B$) while for B and C (high misorientation angle boundary) are very different ($y_B << y_C$). As oxidation progresses (t_2), the areas of initially thinner oxide catch up those which grew at a faster rate, hence stress at the oxide–oxide interface is generated. Through this mechanism, the grain boundary discontinuity is reflected as a mirroring oxide discontinuity on the surface [101].

3.2.5. Intergranular sites

Intergranular sites, such as twins and sub-boundaries, provide regions of metal lattice distortion and therefore low energy nucleation sites [58,59,65,95], and regions of unequal oxide growth resulting in an inhomogeneous oxide layer. These features are considered to arise in

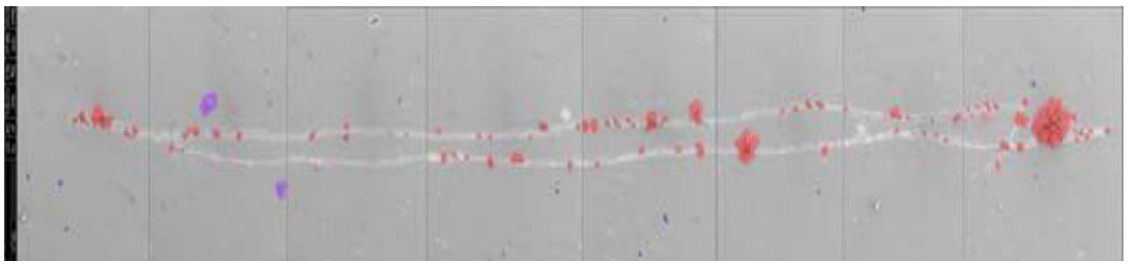

Fig. 9. A series of stitched secondary electron (SE) images of the middle of the scratched area on the sample. Areas of deuteride growth on the scratched material are highlighted in red. Growth areas on the undisturbed uranium surface not positively identified as deuteride growths are highlighted in blue. Areas positively identified as deuteride growths are marked in purple. Stitching lines between secondary electron images are marked by horizontal grey lines. Graph reproduced from reference [102].

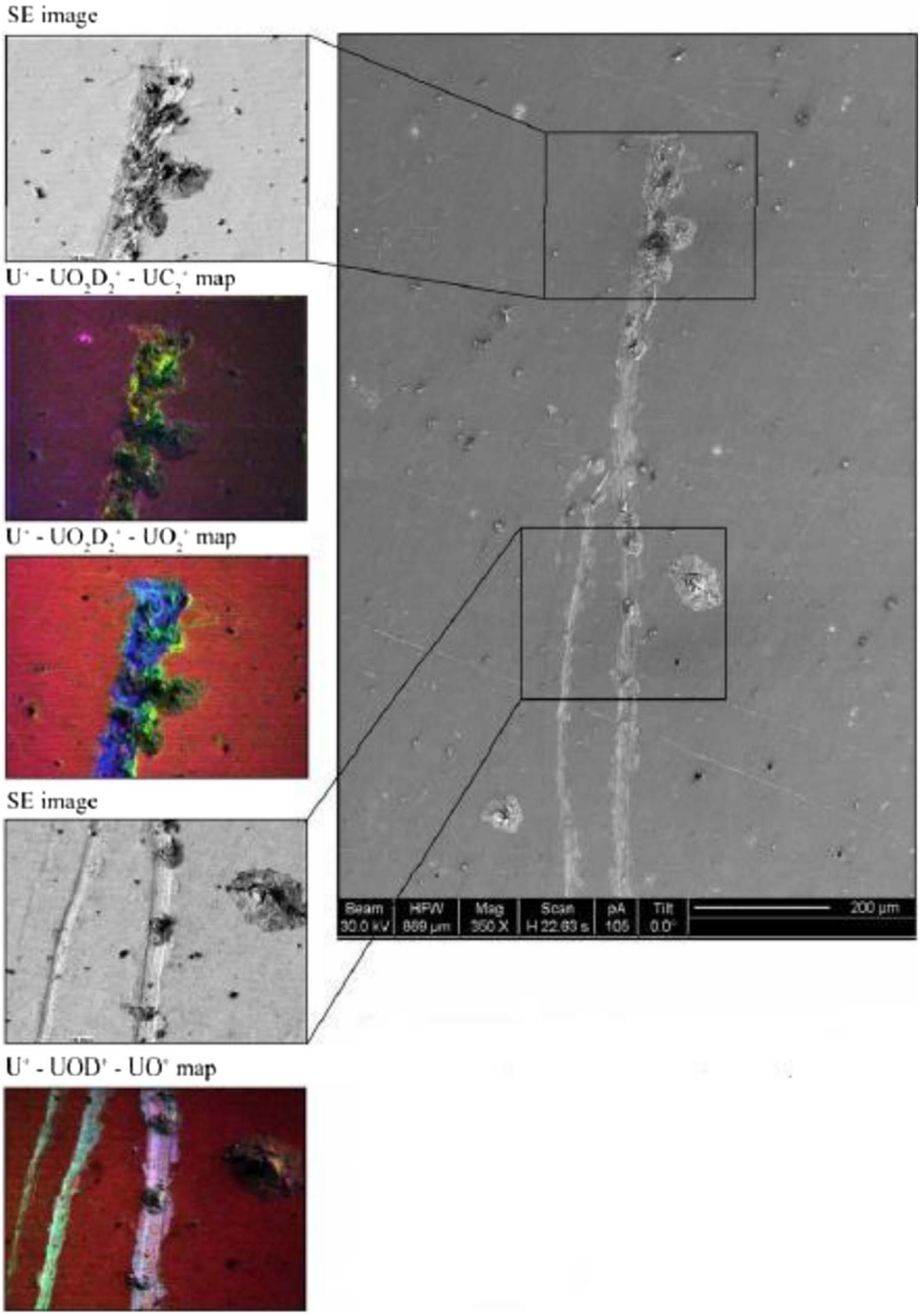

Fig. 10. Secondary electron (SE) images and colour combination ion maps of deuteride growths on the surface of a scratched uranium surface. Maps are RGB (red, green, blue) combinations of the recorded ion maps listed overlying a SE image. The maps clearly show the strong association of deuterium with the observed surface growths. Mapping also shows apparent concentrations of deuterium in small (< 5 µm) discrete patches along the length of the disturbed areas. Graph reproduced from reference [102]. (For interpretation of the references to colour in this figure legend, the reader is referred to the web version of this article.)

response to strain induced on the metal surface as a result of its preparation or from rapid phase change due to quenching from high temperature [83,103]. Filiform-like hydride branches have been observed to run along {130} and {172} crystal planes, the two most common slip systems in uranium metal [59], so suggesting the reaction follows twin boundaries [65] (Fig. 17).

3.3. Growth of hydride sites

The UH_3 nucleation rate tends to follow a Gaussian dependence, peaking at 7–10% surface coverage, then decaying to zero, due to further reaction resulting almost exclusively at already established hydride sites [44,46]. This localised attack acts increase the proportion of metal susceptible to reaction as an irregular surface topography is produced. Due to the considerable density difference between UH_3 and uranium metal [104], Table 1, resulting in a ~1.75 × volume expansion upon reaction, strain fields accompany the reaction [105] and may contribute to perpetuating the growth of already existing hydride.

Due to the ductility of uranium and the brittle nature of the reaction product, the hydride fractures and spalls as a fine black powder [4,106]. This has led to the suggestion that the rate-limiting step for the reaction occurs at the metal-hydride interface [46]. Any overlying

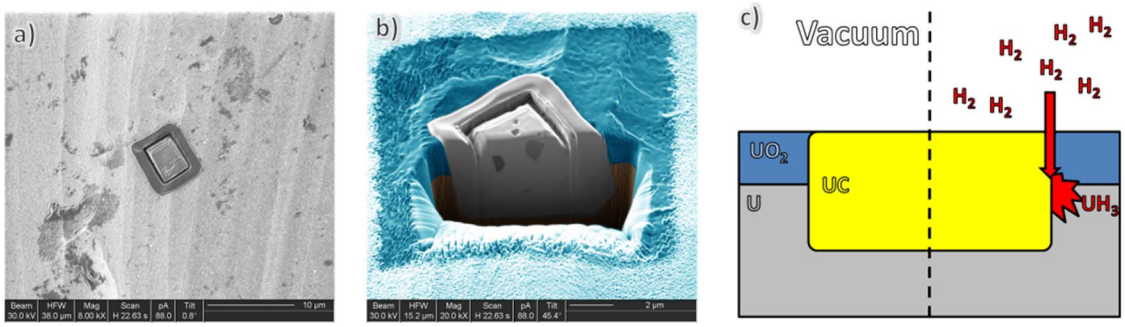

Fig. 11. Secondary electron (SE) images of an inclusion in uranium metal and a schematic showing how they offer preferential sites for hydride growth nucleation. (a) A SE image of a typical inclusion at the surface of uranium. (b) A cut section through the same inclusion showing the inclusion is penetrating a thick oxide layer (highlighted in blue) (> 1 μm) that resides on the metal surface. (c) A schematic showing how the carbide-metal interface may allow hydrogen to bypass the oxide layer and so making inclusions preferential hydride nucleation sites. Graph adapted from [13] and reproduced from reference [102]. (For interpretation of the references to colour in this figure legend, the reader is referred to the web version of this article.)

surface oxide is split and forced apart by the UH_3 forming beneath, providing a direct pathway for further ingress of hydrogen. This direct route is then more preferable for hydrogen ingress due to the ionic character of UH_3 bonding (higher than the U—H bond) [107]. As a consequence, it has been reported that the reaction follows a step like procedure, attributed to the accumulation and subsequent release of stress [42].

3.4. The bulk reaction

The individual hydride sites experience linear lateral growth and eventually overlap [42] engulfing the metal surface. Once the surface sites coalesce, the bulk reaction begins, following a decreased, linear kinetic regime [51], propagating into the metal, following a 'contracting envelope' or 'shrinking core' function [47]. Under steady state conditions the UH_3 layer moves into the bulk metal at a fixed velocity and with a constant adherent thickness [108] and numerous models have been produced to describe the reaction [24,28,37,51,68,109–112].

Due to the volume expansion and lack of coherence of the corrosion product, stress cracking occurs, causing the hydride to spall along planes parallel to the metal surface. At the nanoscale, the volume expansion associated with the reaction causes cracking in the parent metal which accelerates the rate of H_2 ingress to the metal in these areas [108].

For a reacting surface area of constant size, the reaction rate generally varies linearly with time at low temperatures; this behaviour may be related to the formation of a constant-thickness adherent hydride layer beneath the continually spalling hydride. The value of the apparent activation energy deduced from rate versus 1/T curves appears to reduce with increasing temperatures due to the increasing dissociation pressure of the hydride as the temperature increases. So, for a constant applied hydrogen pressure, the H^- ion concentration gradient across the adherent hydride layer continually decreases with increasing temperature. This effect partially negates the increasing H^- ion diffusion coefficient in the hydride with increasing temperatures, so giving a reduced value for activation energy. For typical uranium samples exposed to hydrogen, the reacting area generally varies with time during the early stages of the reaction. This variation is reflected in a changing reaction rate until complete coverage of the sample is attained. Rate curves tend to follow a decelerating parabolic curve for high temperatures that becomes 'S' shaped at lower temperatures [51,69], indicating an initial reaction period followed by a bulk reaction stage. This is highlighted in Fig. 18 which shows a schematic graph of the $U + H_2$ reaction for a range of temperatures following pressure (gas consumption) over time. Bulk reaction rate and velocity of the hydride reaction front can also be enhanced by annealing at temperatures > 450 °C. This phenomenon is assumed to relate to grain size increase due to heat-induced microstructural changes in the metal [83,113].

The reaction rate is observed to have a decreasing pressure dependence with increasing hydrogen pressure [51]. For moderate pressure conditions, a half-order dependence has been recorded [37,114]. This observation designates dissociation and diffusion of atomic hydrogen to the metal bulk as being the driving influence. This experimental observation was mirrored by modelling results from Taylor and Lillard [115] who confirmed the thermodynamic preference of dissociated H diffusion on an α-U (001) surface using density functional theory (DFT) [115]. At constant hydrogen pressure, increasing reaction temperature causes a decrease in the hydriding rate [114] giving an apparent negative activation energy of $-6.65\,kJ\,mol^{-1}$. As the applied hydrogen pressure reaches the adsorption equilibrium pressure (i.e. high temperatures or low pressures) kinetics also slow as the decomposition reaction begins [46]. This approach to equilibrium and the decrease in reaction rate has been observed by numerous investigators [24,51,83,110]. At pressures much greater than equilibrium, pressure independence is exhibited [24,51,111]. Recent experimental work by Stitt et al. [116] working on hydriding of uranium in grouted systems has shown that the temperature of the reacting metal may play a more influential role in early UH_3 formation than the temperature of the gas as previously believed (Fig. 19).

The body of evidence, from both modelling and experiments, indicates that the physical characteristics of both the surface oxide and underlying metal are important for dictating the hydride formation behaviour. For storage applications it is therefore valuable to understand both the elemental make-up and microstructure of the metallic uranium (which is informed by its fabrication and in-reactor history) as well as its current state of corrosion, including the thickness and stoichiometry of the enveloping oxide and the relative abundance of hydride as a proportion of the total mass of corrosion product.

4. Additional effects on the rate of the $U + H_2$ reaction

4.1. U-Alloying

Much of the emphasis of UH_3 research has been directed at better understanding its formation on exposed α-U metal surfaces. However, one of the intrinsic properties of all metals is the level of impurities and the hydrogen content they acquire during the fabrication process [117].

4.1.1. Hydrogen content versus embrittlement in pure uranium

At low concentrations, hydrogen may be accommodated in uranium by impurities like carbides [118,119], as absorption and trapping at these sites is thermodynamically more preferable [120]. At higher contents, hydrogen is diluted in uranium up to the point where UH_3 precipitates start to form [119,121]. It has been postulated that for any uranium metal there may be small, micron-sized (or smaller) hydride

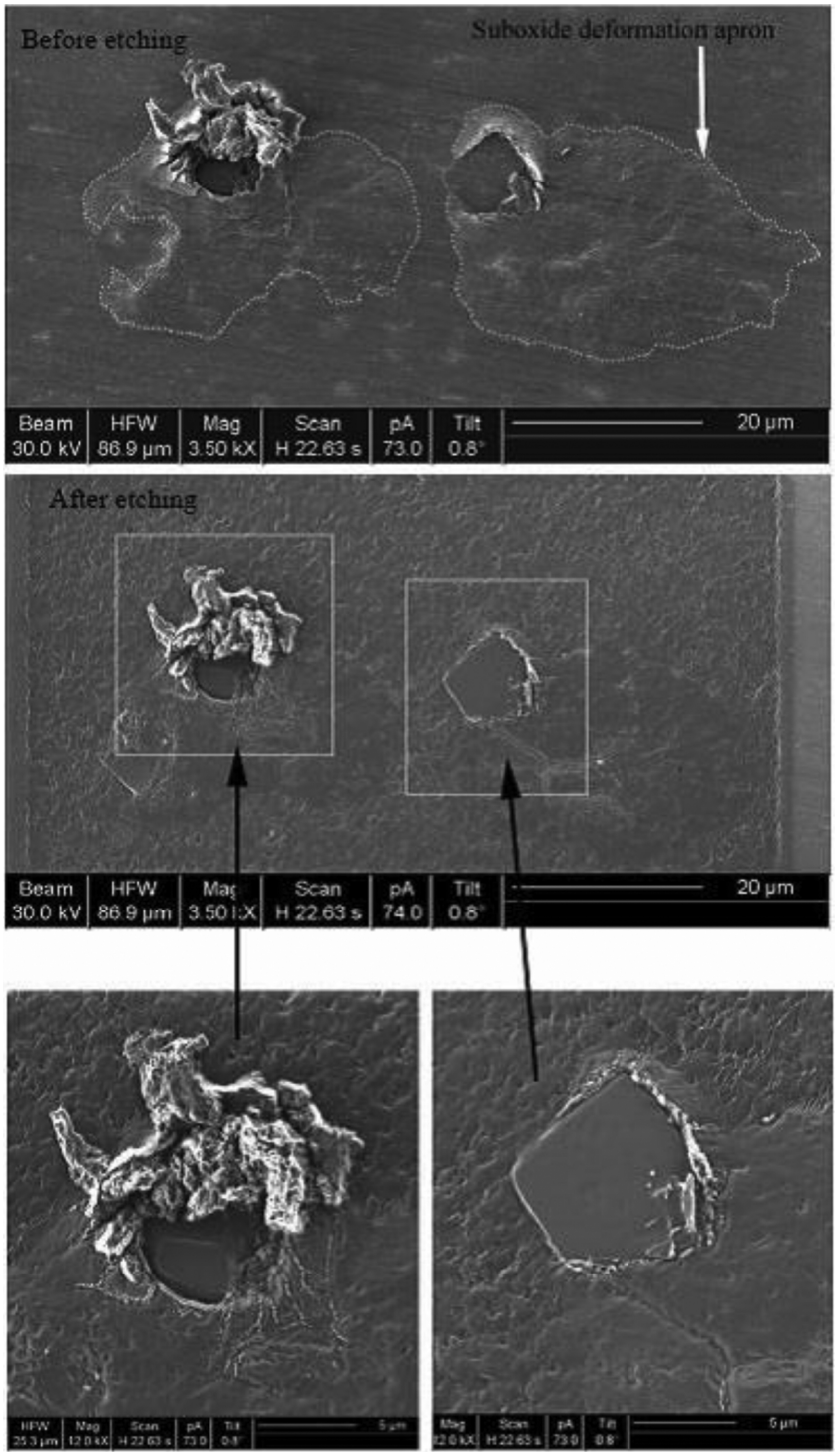

Fig. 12. Secondary electron (SE) images, before and after ion etching, of hydride formed around a pair of carbo-nitride inclusions showing the apron of deformed oxide surrounding the UH_3 growths.

precipitates, finely disseminated throughout the microstructure [118] formed during initial crystallisation of the metal from a molten state. Grain boundaries have been addressed as initial locations for hydrogen trapping [121], however, this assumption is disputable [122]. It is notable that the ductility of uranium decreases significantly when the hydrogen content exceeds 0.5 ppm [120] with maximum embrittlement observed at 2.5 ppm hydrogen [123], implying an influence of grain boundary UH_3 precipitates. The loss of ductility as an effect of UH_3 precipitation and other impurities can also be directly correlated with enhanced hydriding kinetics [120].

4.1.2. Other alloys

Across the literature, there are a respectable number of investigations of the hydriding reaction for various uranium alloy compositions. Low alloying can be either unavoidable as part of the manufacturing process (Al, C, Cr, H_2, Si, V, etc.) or deliberate to enhance the performance of the material (Nb, Ti). Uranium-chromium and −vanadium alloys were found to react faster than pure uranium during hydrogen exposure [42,64]. Carbon and silicon contents along with the various thermal treatments are regarded as controlling mediums of the grain size with the higher content resulting in finer grains [117]. However,

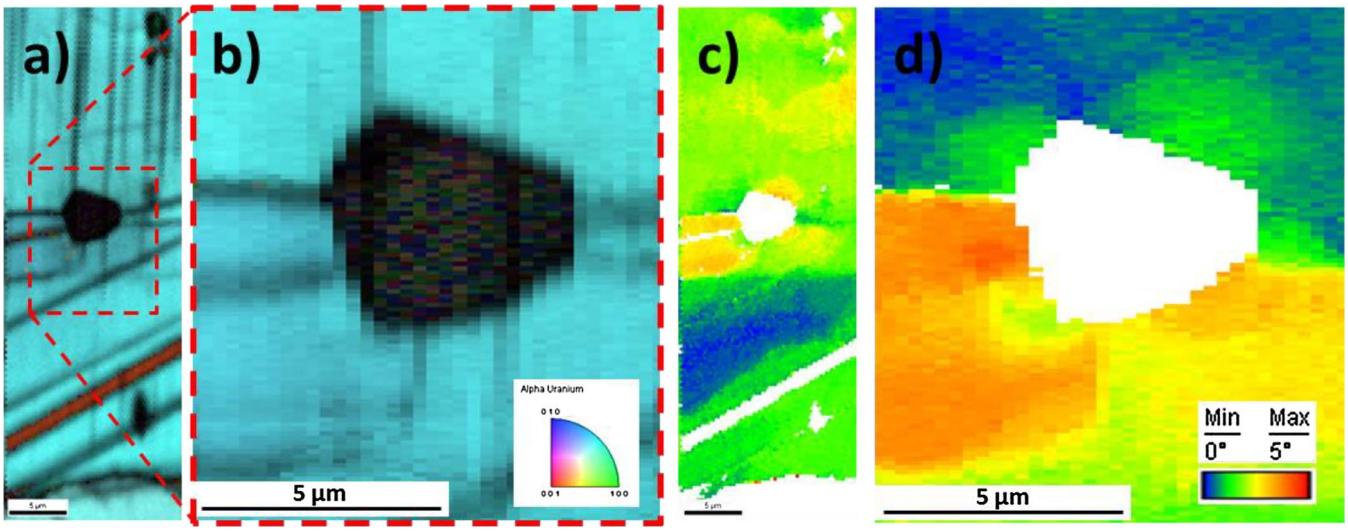

Fig. 13. (a & b). Two separate datasets displaying combined image quality and crystal orientation data with a corresponding inverse pole figure (bottom right of figure a) of α-U surrounding the same inclusion. Each has a similar scan time but the left-hand image covers a much larger area. The orange line running diagonally across the lower half of the left-hand figure is a crystal twin and aligns with other dislocation planes above and below it. (c & d) inter crystal variation maps of the data sets shown in (a & b). The colour scale indicates up to 5° misorientation from a reference crystal orientation taken from the bulk, in an area assumed to be unstrained (blue). Misorientation exists across the mapped area, but the inclusion acts as an obvious focal point, affecting an area of radius ~ 5 µm from its perimeter, causing ~ 1° orientation change as the inclusion metal interface is approached. Graph adapted from [13] and reproduced from reference [102]. (For interpretation of the references to colour in this figure legend, the reader is referred to the web version of this article.)

silicon at elevated content (> 100 ppm) increases the hydriding kinetics by promoting spalling across the metal lattice [113]. Niobium is a well-known additive used to increase the oxidative corrosion resistance of the material. Contrary to their oxidising behaviour with O_2/H_2O, U-Nb alloys respond with more complexity to hydrogen corrosion with U-2.5 wt% Nb reported to react faster than pure uranium, but U-5.7 wt% Nb to appear significantly more resistant to corrosion [53]. This may be partly influenced by the phase composition of the alloy which transitions from an orthorhombic α-phase to a γ-phase at ~6 wt % Nb. Similar influences have been observed in the U-Cr system where β-quenched alloy have been observed to show enhanced hydriding kinetics[103]. Finally, titanium was recognised as an additive that increases the life-performance of the uranium-fuel to both oxidising and hydriding environments due to its stainless properties [58]. This alloy has since found widespread use in artillery and other military ordinance.

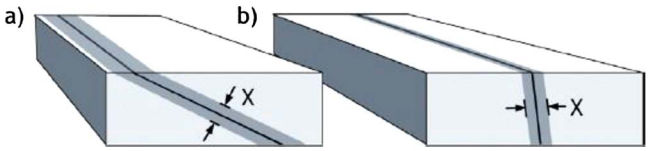

Fig. 15. A schematic diagram showing the effect of grain boundary orientation relative to the metal surface. Although the width of the boundary remains the same in both cases (a & b), the width of disordered material exposed at the surface varies, depending and the angle of the boundary. Figure reproduced from [65].

4.2. Surface passivation

For the nuclear industry, the prospect of hydride formation in bulk quantities is undesirable. Accordingly, several studies between 1983 and 2006 have examined the possibility of coating or altering the uranium surface to prevent corrosion. In an effort to delay if not prevent

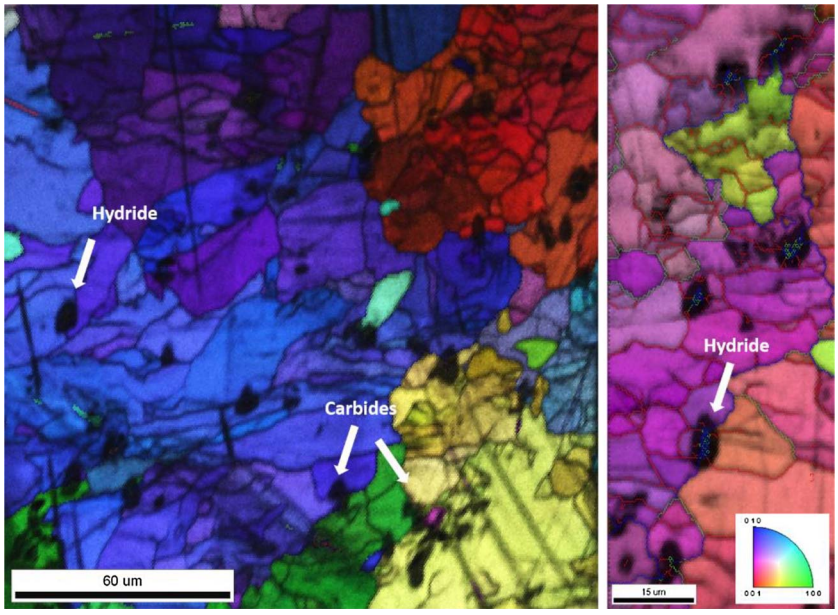

Fig. 14. Electron back-scattered diffraction (EBSD) maps of Magnox natural uranium which is mechanically polished, electropolished and partially hydride. The blurry black spots represent either hydride growth locations or carbide inclusions. Secondary electron (SE images) combined with mass ion maps of the same mapped regions allowed us to resolve the hydrides from the inclusions and statistically analyse the UH_3growth locations. Figures reproduced from reference [102].

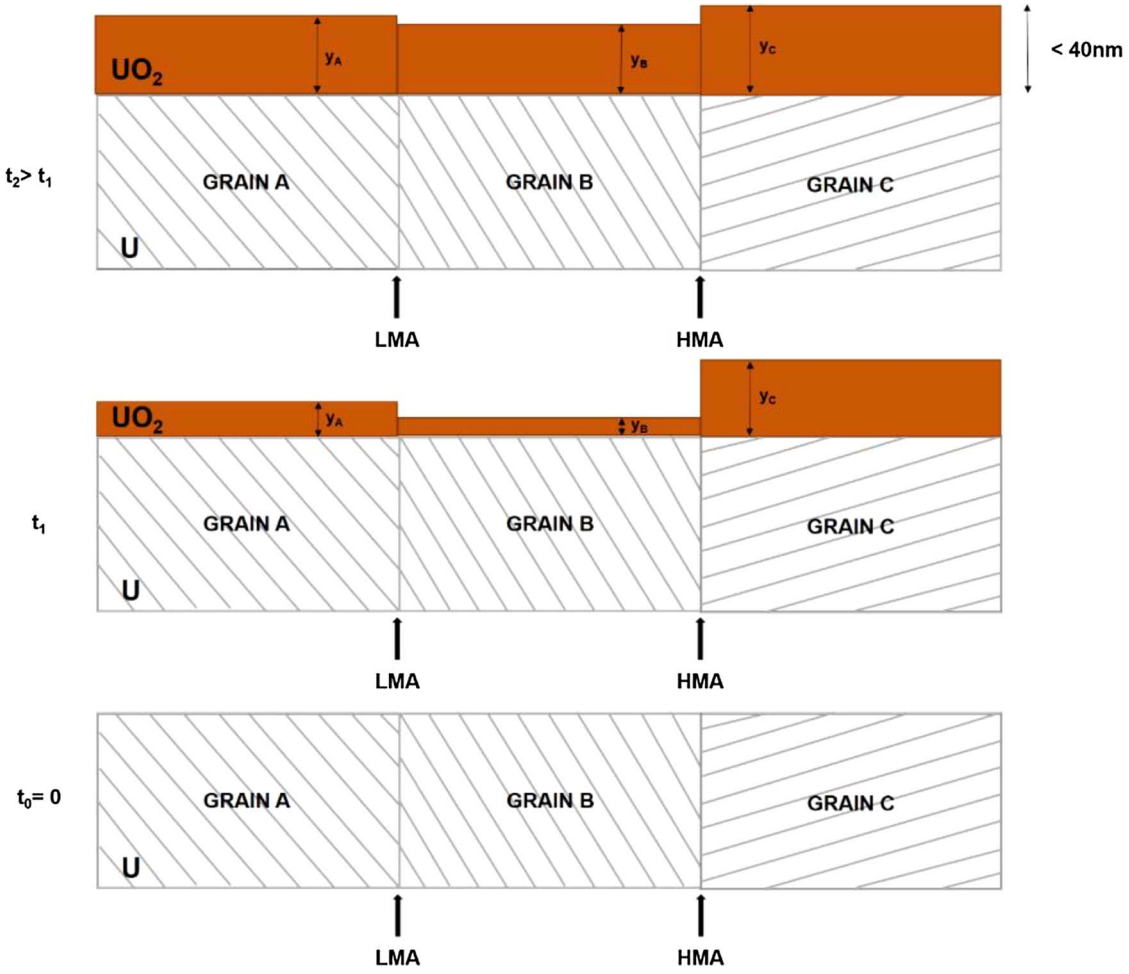

Fig. 16. Schematics showing how the oxidation kinetics progresses on grains with different rotational mismatch. As the oxide of the initially slower oxidising grains thickens to catch up the other ($t_1 \rightarrow t_2$), stress is generated on the oxide–oxide interface. LMA and HMA refer to low misorientation angle and high misorientation angle boundaries, respectively. Schematics reproduced from [101].

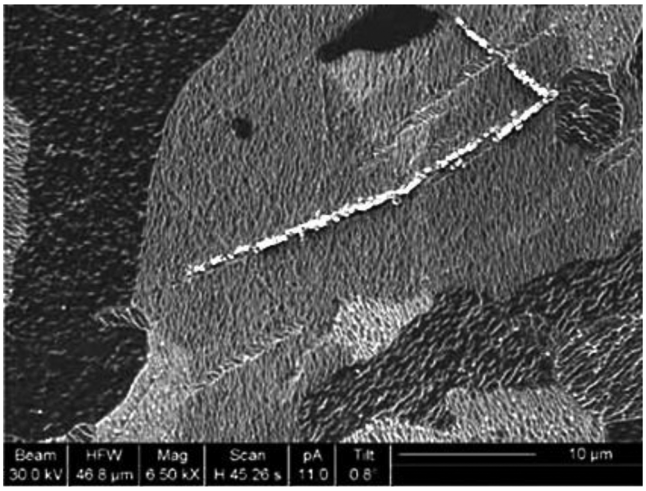

Fig. 17. Showing hydride growth along an intergranular twin. The sample was reacted at 320 °C and 500 mbar D_2. The oxide layer was subsequently removed via ion etching to reveal the metal subsurface. Figure reproduced from [65].

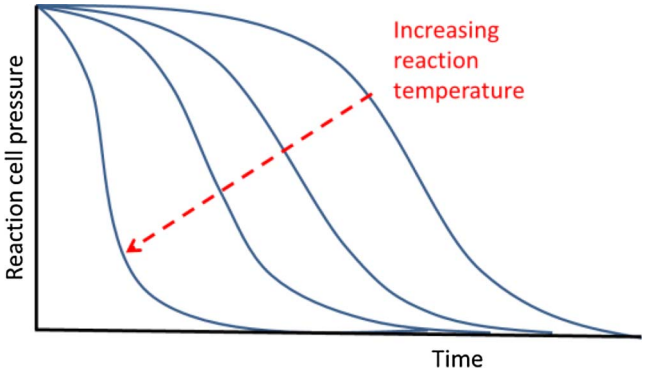

Fig. 18. A schematic graph showing the effect of temperature on the U + H_2 reaction. The assumed reaction is occurring in a fixed volume of H_2 gas, hence the pressure decreases with time. Figure reproduced from reference [102].

this reaction, ion-surface implantation has been employed [124–131]. Oxygen [125,131], carbon [126,128–130], nitrogen [127–129] and sulphur [128] ions have all been investigated as passivating agents. All studies have shown that the induction period was extended, and the reactive surface was minimized to site-specific regions leaving a large fraction of the implanted surface unaffected. However, except for sulphur, stress build-up was recorded in the uranium lattice as result of implantation which persisted even after the surface implanted layer was nominally removed [128].

4.3. Strain

In a variety of other metallic systems, corrosion is recognized to be influenced by tensile or compressive loading (stress), commonly

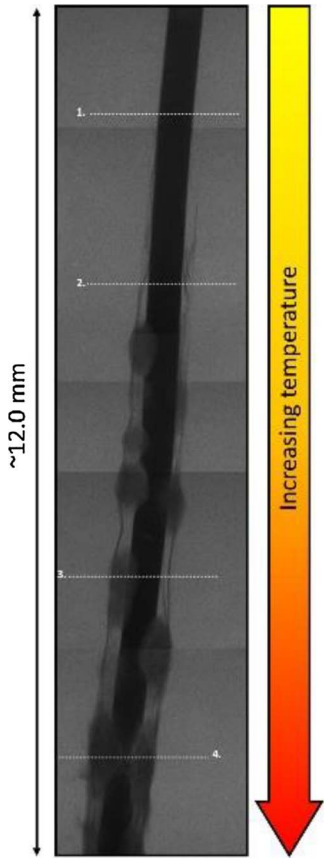

Fig. 19. A set of consecutive radiographs exhibiting the grout encapsulated uranium rod (black) and resulting corrosion products (dark grey) through the temperature gradient. The warmest temperatures were exposed to the base of the sample and the temperature cooled with distance away from this region. The numbered lines correspond to the XRPD line scans. Figure reproduced from [116].

referred to as stress corrosion. In uranium, this phenomenon has not been well explored.

Internal, external, surface and interface stresses are introduced to the material during the fabrication [132,133], preparation [96,102] and even during corrosion [134]. The generated strain, which is defined as the amount of deformation at distinct intervals of tensile or compressive loading, can be categorised into three distinct types:

i **Internal strain.** Stresses developed in the metal during the various thermal and mechanical preparations during manufacturing. These deformations are produced when the elastic flow is exceeded and plastic deformation occurs [132]. The latter may arise as a result of anisotropic thermal contraction between the grains and the surrounding aggregate during cooling after a thermal process (casting, β-quenching etc.) [133]. These stresses are commonly reflected as slip and twinning modes on the metal lattice. The (001)[100] slip mode is the primary system observed for uranium at room temperature [132]. There are 41 twinning modes identified for uranium and for simple shuffle mechanisms [135], with the most commonly detected to be the {130} ⟨310⟩ and '{172}' ⟨312⟩ systems [99]. It was shown in section 3.2.5 that these sites serve as preferred locations for hydride nucleation and growth.

ii **External strain.** These include the residual stresses on the surface after mechanical preparation, leaving a work-hardened layer e.g. cutting, grinding or polishing. Recent work has confirmed that polishing scratches facilitate hydride formation [96,102] and that a disrupted work-hardened layer transforms the reaction behaviour to be more rapid locally [94].

iii **Corrosion generated strain.** When oxidation occurs at the uranium surface the difference in density between the oxide and the underlying metal generates in-plane compressive stresses in the SPL and tensile stresses in the metal lattice. Stress is at the highest level at the metal-oxide interface and diminishes vertically away from it [136]. This strain can be relieved with cracking and flaking of the SPL which again modifies the reactivity of the metal towards hydrogen [56]. Differential volume expansion is also a driving stress generator when nucleation of hydride growths occurs [60,134,137]. The stress is partially relieved when hydrides breach the SPL [134] or by hydride 'streamers' moving into the bulk of the metal [90].

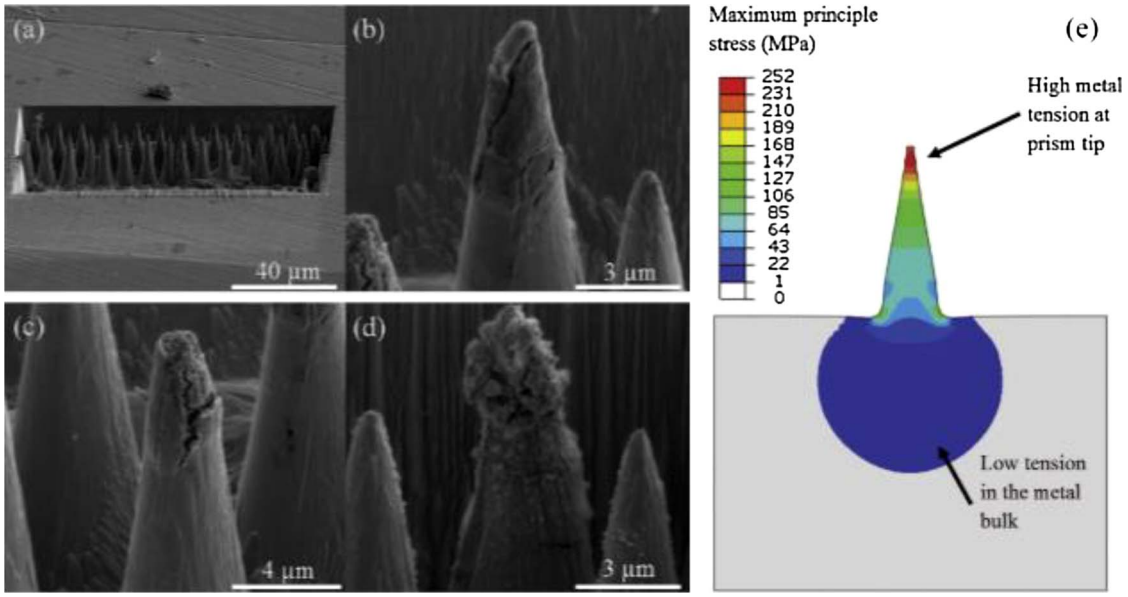

Fig. 20. SEM images of the pillars after reacting with 12 μmol of D_2. (a) Shows the entire array and (b)–(d) individual pillars that have commenced UD_3 nucleation on their apex. (e) Finite element modelling showing the distribution of tensile stresses induced by the loading of uniform oxide growth. The scale is represented in maximum principle stress (MPa); the red end of the colour spectrum indicated zones of high and blue low tensile stresses. Figures reproduced from [139]. (For interpretation of the references to colour in this figure legend, the reader is referred to the web version of this article.)

Hydrogen embrittlement and alloying additions are inseparably linked with induced stresses; however, it is uncertain how strain affects the hydriding kinetics. Several DFT studies have mentioned that tensile/expansive forces in the metal could act to further enhance UH_3 formation while the reverse (compressive forces) could possibly result in reaction deceleration on the stage [115,138]. Stitt et al. [139] have worked on the early hydriding of uranium which was cut into a series of pillar shapes using ion beam milling (Fig. 20a). The study observed that UH_3 has first initiated at the apex of these features where tensile forces were considerably higher in value with regards to the rest of the bulk (Fig. 20b–e). Equally, these apex regions were geometrically predisposed to preferential hydride formation and hence it is not possible to extricate which parameter exerted the greater control on early hydride formation.

Operationally the experimental data suggests that uranium metal that has been mechanically worked or strained as part of in-reactor burn-up is likely to exhibit a different corrosion behaviour, both for oxidation and hydriding, relative to an unstrained counterpart [94,96].

5. Dehydriding

As previously set out in Eq. (1), the hydriding reaction may be reversed if H_2 gas is removed and the temperature increased, usually done most effectively in vacuum. The point at which hydriding ceases and dehydriding begins is dependent on temperature and pressure, with the change point highly dependent on the means of measurement [9]. Empirically, the decomposition pressures of UH_3, UD_3 and UT_3 have been given as:

$$\log P = -\frac{A}{T} + B \tag{2}$$

For P is in torr, T is in kelvin (K), $A = 4500$ K, $B = 9.28$ for UH_3, $A = 4700$ K, $B = 9.46$ for UD_3 and $A = 4471$ K and $B = 9.46$ for UT_3 [9].

Reported values for the activation energy for UH_3 decomposition E_α ranges from $39.7 \pm 2.5\,kJ\,mol^{-1}$ [114] to $79.08 \pm 7.5\,kJ\,mol^{-1}$ [9,37,140] depending on the study, though all have found the rate to obey zero order kinetics. Recent theoretical studies by Lillard et al. [140] also deduced that the rate of dehydriding appears to be unaffected by the conditions under which the hydride was initially formed [140].

A study of the dehydriding of uranium following reaction with water vapour identified the following three regions of hydrogen release when heated from 0 up to 600 °C [141]:

< 250 °C: Release of hydrogen adsorbed on or inside the oxide surface, trapped on oxide grain boundaries or (to a lesser extent) inside the oxide lattice.

~250–400 °C: Release of hydrogen stored as UH_3.

> 500 °C: Removal of hydrogen formerly dissolved (in solution) in the metal [142].

The material product of full dehydriding is a finely divided metallic powder consisting of micron-sized particles. This material is as equally pyrophoric as parent hydride. It is suggested that if dehydriding is only partially complete, particles may exhibit a UH_3 core that is encapsulated by uranium metal. As vacancy formation in the UH_3 core occurs, concomitant with structural changes in the metal, the rate controlling step for dehydriding, then, would be the diffusion of hydrogen through the metal to the uranium surface where it can then desorb into the gas phase.

Whilst there is relatively little published in the public domain regarding the dehydriding behaviour of uranium hydride, such research is potentially beneficial for both storage and SMR applications. For the former, it may be a consideration that for some uranium–containing wastes considered very likely to contain substantial UH_3, a thermal dehydriding treatment followed by controlled dry oxidation may be an appropriate but somewhat complex waste treatment strategy. For the latter, the dehydriding kinetics are important for predicting the breakdown rates over multiple charge-discharge cycles within a reactor core allowing more accurate modelling of reactor self-regulation for temperature and criticality.

6. The production of UH_3 with water

The reaction between uranium and water vapour has been well documented and the presence of UH_3 as a corrosion product is generally [38,39,74,79,143–147] but not universally accepted [33,148]. The role of hydrogen in the reaction remains uncertain. If the reaction occurs in a closed system (e.g. uranium containment in sealed drums), over time the environment becomes H_2-rich (uranium oxidation by H_2O releases H_2 in the gas phase), increasing the likelihood of UH_3 formation via the usual gas metal reaction. It has been recently clarified experimentally that the hydride can form as part of the $U + H_2O$ reaction mechanism (and not just as a separate $U + H_2$ reaction) [149]. Martin et al. [149] used atom probe tomography (APT) to examine the oxidation reaction of uranium by both normal and deuterated water vapour at an atomic/nanoscale. They observed a very thin (3–5 nm) interfacial hydride layer forming at the metal oxide interface just under the hyper-stoichiometric oxide layer. These findings were confirmed by both 3D atom probe maps (Fig. 21a–c) and proximity histograms (Fig. 21d) on the metal oxide interface.

This observed interfacial hydride layer may be considered as 1) a standard solid reaction product for all uranium and oxygen-free water reaction systems and 2) as operationally 'harmless' owing to its constant thickness and action to work as a reaction front, consuming the metal while simultaneously producing more UO_2. It may be assumed that this hydride is potentially amorphous, though its limited thickness (3–5 nm) would make it very difficult to verify.

By comparison, the most problematic type of hydride is considered to be 'bulk' hydride which has formed in significant mass and with a large exposed surface area. That hydride type is mostly produced in enclosed systems where the generated hydrogen gas from U-oxidation cannot diffuse out to the environment but stays trapped in the near uranium metal surface. Water-formed UH_3 produced in an enclosed system has been encountered by investigators opening steel drums containing used fuel [150] and also determined experimentally [151]. The presence of water on such a system affects the duration of the induction period but not the subsequent rate of hydride formation after UH_3 initiation [152]. Environments such as cooling ponds and silos are considered as quasi-enclosed systems due to the complex way that the material is interim-disposed, causing hydrogen to build-up in pressure locally. These areas contain large amounts of intermediate level waste (ILW) such as U-contaminated fuel cladding, conditioned SNF parts along with other metals. The continuing oxidation of this material produces an excess of hydrogen gas that can only partly escape to the environment. If excess trapped hydrogen is generated near uranium, the reaction behaves as an enclosed system. UH_3 forms on such a system and is found to persist over time, even under a water-rich atmosphere [102,153].

In our laboratory, we tried to mimic these conditions by leaving a Magnox-uranium coupon to react with distilled/purified water under vacuum contained and immersed conditions for a long time period at different temperatures [102]. Fig. 22a provides a SIMS depth profile of the reacted surface of uranium in water at 70 °C for 330 h. From the graph, an almost bell-shaped line for the UH^+ intensity signal may be observed as the oxide surface is etched. The UH^+ signal which represents the hydride or hydrogen-rich phase attains its maximum value at t_3 very close to the point where the $UO_2{}^+$ and U lines intersect (metal-oxide interface, t_3) and then decreases in value. Based on the data from Fig. 22a, a simplified 2D illustration showing the cross-sectional face of the sample was produced (Fig. 22b). To provide more definitive proof and support these findings, the sample was subjected to a final three step desorption process while using RGA to analyse the

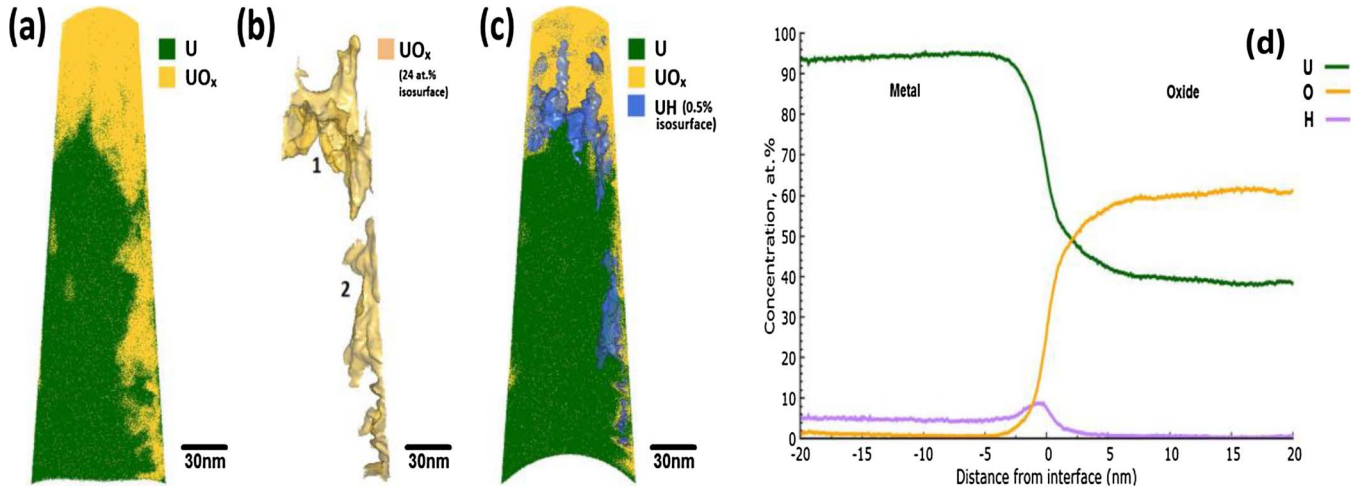

Fig. 21. (a) An atom probe map of a tip extracted from a uranium sample exposed to air for approximately 1 h, showing U and UO_x ions in green and yellow/orange, respectively. The original surface of the uranium is located at the top of the specimen. (b) A 24 at.% UO/UO_2 isosurface indicating two oxide regions on the specimen; (marked 1) at the original surface and (marked 2) generated on the side of the specimen during sample preparation. (c) The same atom map as in (a), but with an isoconcentration surface indicating 0.5 at.% UH in blue to reveal the locations where hydride ions are detected. For (c), the front face of the dataset is cropped away to show a cross-section of the middle of the specimen. (d) Proximity histogram of the surface oxide feature marked as 1 in Fig. 21(b). All complex ions are decomposed into their constituent elements. Figures reproduced from [149]. (For interpretation of the references to colour in this figure legend, the reader is referred to the web version of this article.)

desorbed gases [102]. Hydrogen started emerging in the head-space at temperatures ≥ 220 °C, comparable to the range responsible for desorption of H_2 stored as UH_3 (~250 °C), as previously confirmed by Danon et al. [141].

Hydrides, hydroxides and hydrated oxides have been found along with oxide resulting from reaction between uranium and liquid or water vapour [102,154]. The presence of hydrogen has not been found to impede the oxidation reaction [79] though trace levels of water vapour have been recorded as slowing the hydriding reaction [42].

7. UH_3 oxidation

Like uranium powder, a UH_3 powder also burns in oxygen [15,16,22,155] making it a particularly unstable material to handle. Ignition and the ongoing combustion at room temperature have been confirmed experimentally by Le Guyadec et al. [15] working in an inert environment. Gaseous and solid and solid-only combustion was observed for UH_3 and uranium powders, respectively. Considerable temperature rise along with volume increase of the powder followed the phase transformation of UH_3/U to U_3O_8 [15]. For uranium storage, this has the implication of unintended pyrophoric events where UH_3 has been unintentionally produced, by leaving metal in the presence of H_2 (i.e. storing with water vapour) which if re-exposed to air, can catch fire [14]. Therefore, the reaction has been modelled to investigate storage conditions [156,157]. Due to the ferocity of the reaction between particulate uranium and oxygen, it is assumed that both materials oxidise in a similar fashion [155] with the reacting ion being O_2^- [14,16,158]. Recent numerical models showed that the $UD_3 + O_2$ reaction is more rapid than the reported rate values of the $U + O_2$ system at room temperature [12,157].

What also is apparent is the stability of spot hydrides in air. All of the images in this review acquired by SEM/FIB/SIMS involved a period of air exposure during transfer between reaction cell and instrument vacuum chamber (~2 min). This stability is attributed to the formation

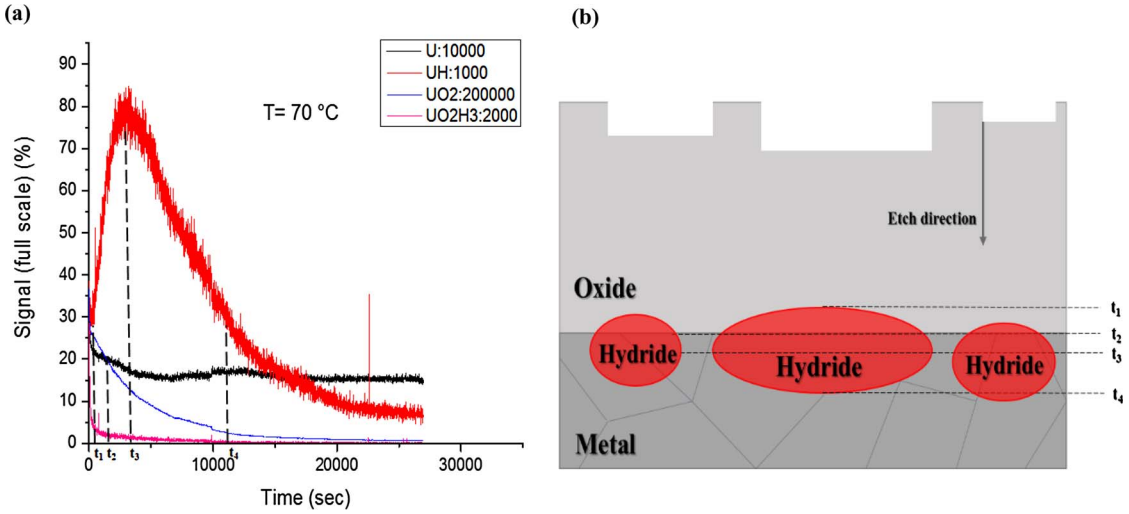

Fig. 22. Showing on (a) Mass ion depth profiling for uranium oxidised in liquid water at 70 °C (Ga+ primary ion beam, 25 keV, 3 nA, positive ion mode, 45° angle of incidence) and (b) a 2D schematics of the cross-sectional view of the same sample by taking into account the data from (a). From the graph and 2D illustration, an almost linear increase in the UH signal (red line) may be observed reaching its maximum value at the metal oxide interface (in the graph- where the blue and black curves intersect). UOH, UOH_3, UO_2H, UO_2H_2 and UO_2H_3 clusters were also traced at and/or near the gas-oxide interface indicating a H_2-rich oxide. Figure reproduced from [102]. (For interpretation of the references to colour in this figure legend, the reader is referred to the web version of this article.)

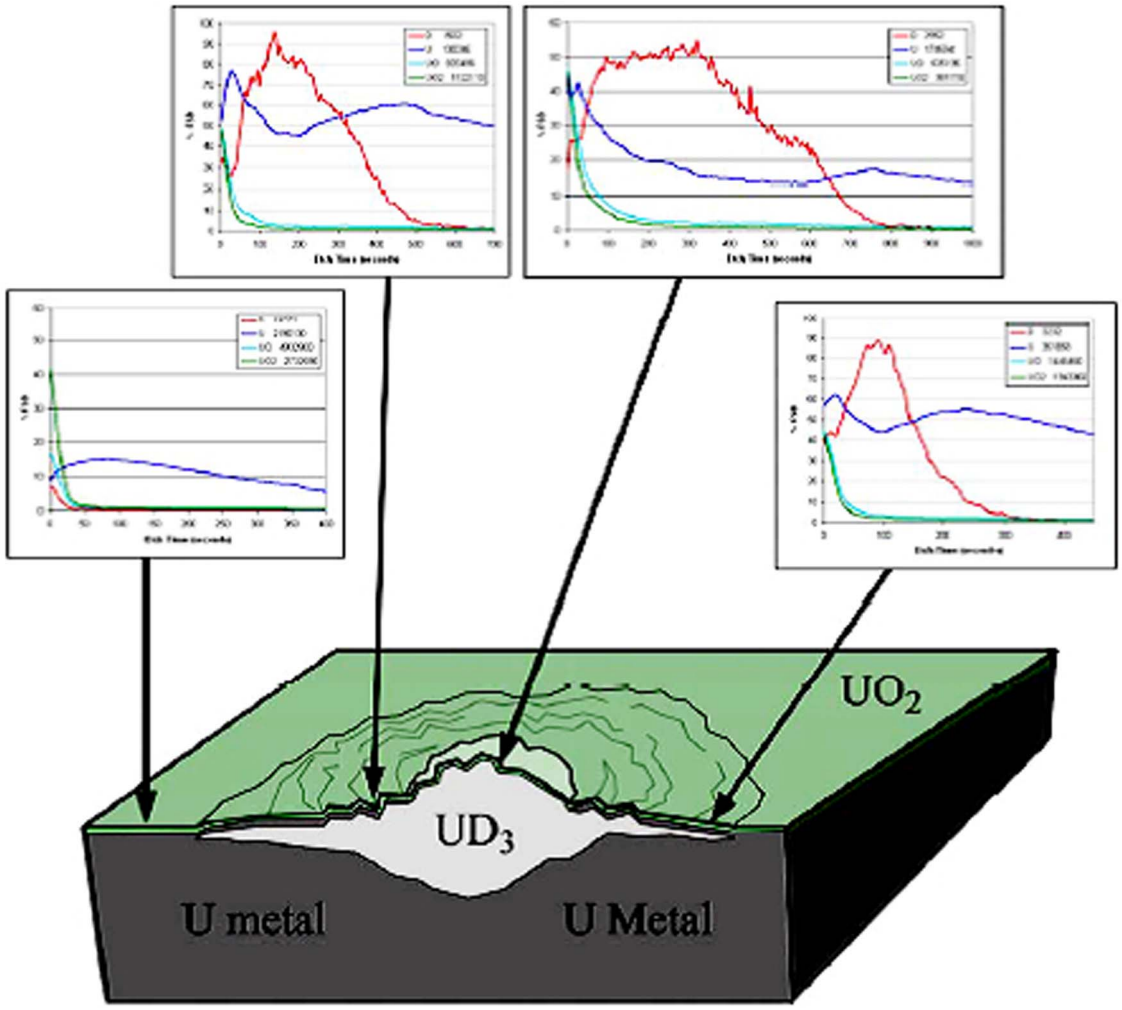

Fig. 23. Positive secondary ion mass spectrometry (SIMS) depth profiles charting the abundance of U^+ (dark blue), D^+ (red), UO^+ (light blue), and UO_2^+ (green) ion clusters with etch time using a 3 nA beam current from different 13 μm^2 areas across a 100 µm diameter hydride growth. The experiment was performed on an annealed DU coupon at 200 °C with 500 mbar D_2 pressure. The reaction was stopped by evacuation of the gas after a 4–5 mbar pressure drop was observed, equivalent to a 1–2% surface reaction. Figure reproduced from reference [102]. (For interpretation of the references to colour in this figure legend, the reader is referred to the web version of this article.)

of a thin uranium oxide layer on the hydride, screening the bulk hydride from further rapid reaction. Due to the low surface area of hydride, the heat generated by oxidation was not sufficient to drive a pyrophoric response [159].

Fig. 23 shows SIMS depth profiles recorded at numerous positions across a hydride site, moving from hydride free metal surface to hydride spot. A primary observation revealed that both the metal surfaces and the deuteride growths were coated with a thin layer of uranium oxide < 50 nm thick (Fig. 21). The oxide layer on the deuterium growths must have developed during the transfer of samples between analysis systems. Ion beam etching and SIMS ion mapping also show that the oxide is more adherent to the hydride sites than to the metal. Fig. 24 shows secondary ion colour maps before and after 30 min etching with a 3 nA beam current. After this time, the metal has been mostly cleared of oxide, whilst the hydride sites which penetrate at short distance into the metal, still retain some of their mass.

To summarise, the nature of the $UH_3 + O_2$ reaction means the following points must be considered when studying or using UH_3:

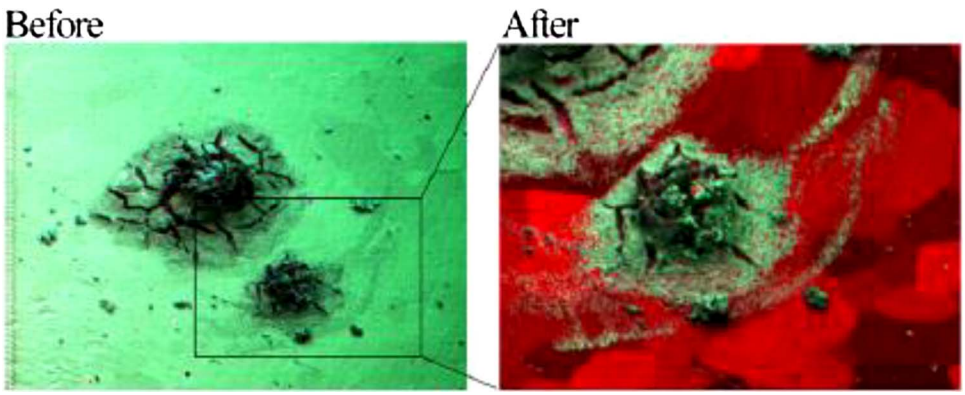

Fig. 24. Positive ion colour combination maps of a deuteride growth before and after etching for 30 min at a 3 nA beam current. Maps are RGB of U^+, UO_2^+ and, UO^+ respectively overlying a SE image clearly showing the oxide remains on the hydride areas despite having been etched from the metal surface. The experiment was performed on an annealed DU coupon at 200 °C with 500 mbar D_2 pressure. The reaction was stopped by evacuation of the gas after a 4–5 mbar pressure drop was observed, equivalent to a 1–2% surface reaction. Figure reproduced from reference [102].

i. For safety UH_3 should be stored and handled in oxygen- and water-free environments to prevent ignition and/or pyrophoric reaction.
ii. If oxygen exposure is unavoidable, factors like exposed surface area [160] and mass of the reactive material [15,16] are proportional to the rate and amount of heat that may be released.
iii. Any UH_3 analysis performed outside of the reaction environment may have experienced some degree of atmospheric exposure. This would result in surface reaction and, due to the exothermic nature of the reaction, potentially provide sufficient heat to induce a phase transformation in the residual hydride, given a significant mass of UH_3.
iv. Likelihood of ignition at room temperature may be reduced by prior controlled exposure to a limited amount of oxygen or moisture [15,16].
v. During dehydriding, the arising metal powder readily reacts with any contaminant oxygen in the system to form an oxide (UO_{2+x}), acting to further purify the released gas. This, however, also has the effect of gradually reducing the hydrogen storage capacity of the metal over time due to the degree of oxide formation. This has significant relevance to uranium used in hydrogen storage beds where multiple loading and unloading cycles may degrade their operational performance.

8. Conclusion

It is now 60 years since the first fission reactor became operational, using uranium metal as fuel. Over this period a significant body of research has been accumulated on the corrosion of uranium metal and the formation and reactivity of UH_3 as one of its potential corrosion products. The current work has attempted to consolidate this significant body of knowledge into a more concise set of observations and descriptions, applicable for both nuclear waste storage and development of SMR concepts based on UH_3 as the fuel material. It is clear that gaps in understanding still exist, specifically in terms of mechanisms for behaviour and for research conducted on real spent fuel materials as opposed to non-irradiated counterparts.

Due to the reactive nature of UH_3, it is challenging to produce a sample and then characterise it 'ex-situ' without guaranteeing some degree of surface reaction. This, combined with the exothermic nature of the reaction which could easily convert α-UH_3 to β-UH_3 suggests there is much still to study in the α-UH_3 system to better understand its fundamental properties and corrosion behaviour. The literature contains a paucity of α-UH_3 data, and that which exists is very old. The majority of the hydride experiments reported in literature relate to the β- form and accordingly it would be academically and industrially interesting to better determine the physiochemistry and mechanical properties of both phases.

Furthermore, an investigation is required largely to determine the nature of the hydride formed under different conditions, along with its subsequent reactivity when exposed to the atmosphere. A thorough understanding of these two related systems would permit operational risk to be more accurately quantified when working with this material.

Additionally, a thorough investigation and determination of the effect of localised stress in the metal on corrosion behaviour is recommended. The recent work on stress corrosion in uranium is tantalising but far from comprehensive. Certainly, it is the case that uranium components are frequently strained, via manufacturing, processing, irradiation etc. If the effect of strain is determined, then by knowing the level of stress, the long-term corrosion behaviour may be better predicted. This would be the case for spent uranium fuel materials, where there is little literature corrosion data available. A comprehensive study of hydride formation on spent/irradiated uranium metal fuel is therefore recommended to provide reaction rate data to better underpin safety predictions of material state in storage.

Acknowledgements

We would like to acknowledge the UK Atomic Weapons Establishment, the Sellafield Centre of Expertise on Uranium and Reactive Metals, the UK Engineering and Physical Sciences Research Council (EPSRC) (Ref: 1338575) and the Royal Academy of Engineering for their funding support for this review. We would also like to acknowledge the affiliation of this work to the EPSRC's DISTINCTIVE research programme (EP/L014041/1), which has led to a significant body of groundbreaking research into nuclear waste management and decommissioning. We would also like to thank Professor Geoff Allen, Dr Joe Glascott, Dr Anna Adamska and Mr John Jowsey for their important support and input.

References

[1] L. Owen, R. Scudamore, A microscope study of the initiation of the hydrogen-uranium reaction, Corros. Sci. 6 (1966) 461–468.
[2] R. Arkush, A. Venkert, M. Aizenshtein, S. Zalkind, D. Moreno, M. Brill, M. Mintz, N. Shamir, Site-related nucleation and growth of hydrides on uranium surfaces, J. Alloys Compd. 244 (1996) 197–205.
[3] J. Glascott, Hydrogen & uranium; Interactions between the first and last naturally occurring elements, Discov. Sci. Technol. J. AWE 6 (2003) 16–27.
[4] T. Totemeier, Characterization of uranium corrosion products involved in a uranium hydride pyrophoric event, J. Nucl. Mater. 278 (2000) 301–311.
[5] H. Yoo, W. Kim, H. Ju, A numerical comparison of hydrogen absorption behaviours of uranium and zirconium cobalt-based metal hydride beds, Solid State Ion. 262 (2014) 241–247.
[6] F. Manchester, A. San-Martin, H.U. The, (hydrogen-uranium) system, J. Phase Equilib. 16 (1995) 263–275.
[7] J. Bloch, The hydriding kinetics of activated uranium powder under low (near equilibrium) hydrogen pressure, J. Alloys Compd. 361 (2003) 130–137.
[8] D. Chung, J. Lee, D. Koo, H. Chung, K.H. Kim, H.-G. Kang, M.H. Chang, P. Camp, K.J. Jung, S. Cho, Hydriding and dehydriding characteristics of small-scale DU and ZrCo beds, Fusion Eng. Des. 88 (2013) 2276–2279.
[9] D. Lindner, Isothermal decomposition of uranium hydride, J. Less Common Met. 157 (1990) 139–146.
[10] N. Kherani, W. Shmayda, A. Heics, Enhancing the rate of hydriding in uranium beds, Zeitschrift für Physikalische Chemie 164 (1989) 1421–1428.
[11] O. Peterson, High Hopes for Hydride (Reprinted from Modern Power Systems, December 2008), WILMINGTON PUBL., WILMINGTON HOUSE, MAIDSTONE, RD., FOOTS, CRAY, SIDCUP DA14 SHZ, KENT, ENGLAND, 2009, pp. 25–27.
[12] M.P. Kanouff, P.E. Gharagozloo, M. Salloum, A.D. Shugard, A multiphysics numerical model of oxidation and decomposition in a uranium hydride bed, Chem. Eng. Sci. 91 (2013) 212–225.
[13] N. Harker, The Corrosion of Uranium in Sealed Environments Containing Oxygen and Water Vapour, PhD Thesis, University of Bristol, 2012.
[14] T.C. Totemeier, R.G. Pahl, S.M. Frank, Oxidation kinetics of hydride-bearing uranium metal corrosion products, J. Nucl. Mater. 265 (1999) 308–320.
[15] F. Le Guyadec, X. Génin, J. Bayle, O. Dugne, A. Duhart-Barone, C. Ablitzer, Pyrophoric behaviour of uranium hydride and uranium powders, J. Nucl. Mater. 396 (2010) 294–302.
[16] C. Ablitzer, F. Le Guyadec, J. Raynal, X. Génin, A. Duhart-Barone, Influence of superficial oxidation on the pyrophoric behaviour of uranium hydride and uranium powders in air, J. Nucl. Mater. 432 (2013) 135–145.
[17] J.C. Warf, N. Baenziger, The Preparation and Properties of Some Mixed Uranium Halides, (1948).
[18] J. Gittus, Uranium-metallurgy of the Rarer Metals, Butterworths, London, 1963.
[19] V. Yemel'yanov, A. Yevstyukin, The Metallurgy of Nuclear Fuel; Properties and Principles of the Technology of Uranium, Thorium and Plutonium; Translation by Anne Foster, Pergamon, 1969.
[20] R. Mulford, F. Ellinger, W. Zachariasen, A new form of uranium hydride1, J. Am. Chem. Soc. 76 (1954) 297–298.
[21] J. Grunzweig-Genossar, M. Kuznietz, B. Meerovici, Nuclear magnetic resonance in uranium hydride and deuteride, Phys. Rev. B 1 (1970) 1958.
[22] F. Weigel, J. Katz, G. Seaborg, J.J. Katz, G.T. Seaborg, L.R. Morss (Eds.), The Chemistry of the Actinide Elements, 1 Chapmann and Hall, London, 1986, p. 361.
[23] Q. Johnson, T. Biel, H. Leider, Isotopic shifts of the unit cell constants of the α and β tri-hydrides of uranium: UH_3, UD_3, UT_3, J. Nucl. Mater. 60 (1976) 231–233.
[24] G. Powell, W. Harper, J. Kirkpatrick, The kinetics of the hydriding of uranium metal, J. Less Common Met. 172 (1991) 116–123.
[25] B. Abraham, H. Flotow, The heats of formation of uranium hydride, uranium deuteride and uranium tritide at 25 °C, J. Am. Chem. Soc. 77 (1955) 1446–1448.
[26] H.E. Flotow, H.R. Lohr, B.M. Abraham, D.W. Osborne, The heat capacity and thermodynamic functions of β-uranium hydride from 5 to 350 K, J. Am. Chem. Soc. 81 (1959) 3529–3533.
[27] W. Bartscher, A. Boeuf, R. Caciuffo, J. Fournier, W. Kuhs, J. Rebizant, F. Rustichelli, Neutron diffraction study of β-UD_3 and β-UH_3, Solid State Commun. 53 (1985) 423–426.
[28] J. Condon, Calculated vs. experimental hydrogen reactions rates with uranium, J. Phys. Chem. 79 (1975) 392–397.

[29] C. Zhang, H. Jiang, H.-L. Shi, G.-H. Zhong, Y.-H. Su, Mechanical and thermodynamic properties of α-UH_3 under pressure, J. Alloys Compd. 604 (2014) 171–174.
[30] I. Halevy, S. Salhov, S. Zalkind, M. Brill, I. Yaar, High pressure study of β-UH_3 crystallographic and electronic structure, J. Alloys Compd. 370 (2004) 59–64.
[31] J. Bigeleisen, A. Kant, Low temperature mobility of hydrogen in uranium hydride. Exchange equilibrium of deuterium between hydrogen and uranium hydride, J. Am. Chem. Soc. 76 (1954) 5957–5960.
[32] E. Fuller, N. Smyrl, J. Condon, M. Eager, Uranium oxidation: characterization of oxides formed by reaction with water by infrared and sorption analyses, J. Nucl. Mater. 120 (1984) 174–194.
[33] J.M. Haschke, T.H. Allen, L.A. Morales, Reactions of plutonium dioxide with water and hydrogen-oxygen mixtures: mechanisms for corrosion of uranium and plutonium, J. Alloys Compd. 314 (2001) 78–91.
[34] F. Caralp-Amilhat, M. Destriau, Changes in the Surface of Uranium and Its Hydrides During Successive Hydrogenations and Dehydrogenations at Various Temperatures, Bordeaux University, Talence, France, 1970.
[35] S. Paek, D.-H. Ahn, K.-R. Kim, H. Chung, Characteristics of reaction between hydrogen isotopes and depleted uranium, J. Ind. Eng. Chem. 8 (2002) 12–16.
[36] M.M. Baker, L. Less, S. Orman, Uranium, Uranium + water reaction. Part 2. – Effect of oxygen and other gases, Trans. Faraday Soc. 62 (1966) 2525–2530.
[37] J. Condon, E. Larson, Kinetics of the uranium-hydrogen system, J. Chem. Phys. 59 (1973) 855–865.
[38] M.M. Baker, L. Less, S. Orman, Uranium + water reaction. Part 1. – kinetics, products and mechanism, Trans. Faraday Soc. 62 (1966) 2513–2524.
[39] M. Bennett, B. Myatt, D. Silvester, J. Antill, The oxidation behaviour of uranium in air at 50–300 °C, J. Nucl. Mater. 57 (1975) 221–236.
[40] C. Broan, Exothermic reaction of samples of uranium corrosion product produced in simulated magnox sludge liquor at 50 °C with air, NNL, 15/11/2011.
[41] D. Bedere, P. Sans, Hydridation of the alloy $UV_{(0.095)}$ in the presence or not of the inhibitor CO, (1983).
[42] J. Bloch, F. Simca, M. Kroup, A. Stern, D. Shmariahu, M. Mintz, Z. Hadari, The initial kinetics of uranium hydride formation studied by a hot-stage microscope technique, J. Less Common Met. 103 (1984) 163–171.
[43] J. Bloch, D. Brami, A. Kremner, M. Mintz, Effects of gas phase impurities on the topochemical-kinetic behaviour of uranium hydride development, J. Less Common Met. 139 (1988) 371–383.
[44] M. Brill, J. Bloch, M. Mintz, Experimental verification of the formal nucleation and growth rate equations–initial UH_3 development on uranium surface, J. Alloys Compd. 266 (1998) 180–185.
[45] M. Brill, J. Bloch, D. Shmariahu, M. Mintz, The incipient kinetics of hydride growth on cerium surfaces, J. Alloys Compd. 231 (1995) 368–375.
[46] J. Bloch, M.H. Mintz, Kinetics and mechanisms of metal hydrides formation – a review, J. Alloys Compd. 253 (1997) 529–541.
[47] M.H. Mintz, J. Bloch, Evaluation of the kinetics and mechanisms of hybriding reactions, Prog. Solid State Chem. 16 (1985) 163–194.
[48] Y. Ben-Eliyahu, M. Brill, M. Mintz, Hydride nucleation and formation of hydride growth centers on oxidized metallic surfaces – kinetic theory, J. Chem. Phys. 111 (1999) 6053–6060.
[49] W. Albrecht, M. Mallett, Reaction of hydrogen with uranium, J. Electrochem. Soc. 105 (1958) 610–611.
[50] W.M. Albrecht, M.W. Mallett, The Reaction of Hydrogen with Uranium Alloy Types, Battelle Memorial Inst., Columbus, Ohio, 1956.
[51] J. Bloch, M. Mintz, Kinetics and mechanism of the UH reaction, J. Less Common Met. 81 (1981) 301–320.
[52] J.P. Knowles, I.M. Findlay, The influence of vacuum annealing on the uranium–hydrogen reaction, J. Alloys Compd. 645 (2015) S230–S233.
[53] R. Li, X. Wang, Effect of niobium additions on initial hydriding kinetics of uranium, J. Nucl. Mater. 449 (2014) 49–53.
[54] P. Loscoe, Transitioning metallic uranium spent nuclear fuel from wet to dry storage, Waste Management Conference (2000).
[55] S. Bazley, J. Petherbridge, J. Glascott, The influence of hydrogen pressure and reaction temperature on the initiation of uranium hydride sites, Solid State Ionics 211 (2012) 1–4.
[56] R.M. Harker, The influence of oxide thickness on the early stages of the massive uranium–hydrogen reaction, J. Alloys Compd. 426 (2006) 106–117.
[57] B. Kasemo, E. Törnqvist, The kinetics of hydrogen interaction with TiHx films, $0 \leq x \lesssim 2$, Appl. Surf. Sci. 3 (1979) 307–328.
[58] P. Shi, L. Shen, B. Bai, D. Lang, L. Lu, G. Li, X. Lai, P. Zhang, X. Wang, Preferred hydride growth orientation of U − 0.79 wt.% Ti alloy with β + U_2Ti microstructure, J. Nucl. Mater. 441 (2013) 1–5.
[59] M. Hill, R. Schulze, J. Bingert, R. Field, R. McCabe, P. Papin, Filiform-mode hydride corrosion of uranium surfaces, J. Nucl. Mater. 442 (2013) 106–115.
[60] J. Bloch, M.H. Mintz, Types of hydride phase development in bulk uranium and holmium, J. Nucl. Mater. 110 (1982) 251–255.
[61] M.H. Mintz, Y. Zeiri, Hydriding kinetics of powders, J. Alloys Compd. 216 (1995) 159–175.
[62] P. Dantzer, E. Orgaz, Hydriding kinetics and the problem of thermal transfer, Zeitschrift für Physikalische Chemie 164 (1989) 1267–1272.
[63] P. Goodell, P. Rudman, Hydriding and dehydriding rates of the $LaNi_5$-H system, J. Less Common Met. 89 (1983) 117–125.
[64] L. Dion, M. Fiot, J. Fontaine, P. Hemet, G. Lozes, Investigations on the hydration of an uranium-0.2 wt.% vanadium alloy, J. Less-Common Met. 121 (1986).
[65] T.B. Scott, G.C. Allen, I. Findlay, J. Glascott, UD_3 formation on uranium: evidence for grain boundary precipitation, Philos. Mag. 87 (2007) 177–187.
[66] J. Bloch, M. Mintz, The kinetics of hydride formation in uranium, IAEC Rep. 53 (2001).
[67] M. Martin, C. Gommel, C. Borkhart, E. Fromm, Absorption and desorption kinetics of hydrogen storage alloys, J. Alloys Compd. 238 (1996) 193–201.
[68] D. Cohen, Y. Zeiri, M. Mintz, Model calculations for hydride nucleation on oxide-coated metallic surfaces: surface-and diffusion-related parameters, J. Alloys Compd. 184 (1992) 11–23.
[69] R. Alire, B. Mueller, C.L. Peterson, J.R. Mosley, Reaction kinetics of uranium and deuterium, J. Chem. Phys. 52 (1970) 37–46.
[70] D.F. Teter, R.J. Hanrahan, C.J. Wetteland, Uranium Hydride Nucleation Kinetics: Effects of Oxide Thickness and Vacuum Outgassing, Los Alamos National Laboratory, New Mexico, USA, 2001.
[71] G. Allen, P. Tucker, Surface oxidation of uranium metal as studied by X-ray photoelectron spectroscopy, J. Chem. Soc. Dalton Trans. (1973) 470–474.
[72] G.C. Allen, J.A. Crofts, M.T. Curtis, P.M. Tucker, D. Chadwick, P.J. Hampson, X-ray photoelectron spectroscopy of some uranium oxide phases, J. Chem. Soc. Dalton Trans. 5 (1974) 1296–1301.
[73] G.C. Allen, R.K. Wild, Auger spectroscopy of uranium, J. Chem. Soc. Dalton Trans. (1974) 493–498.
[74] G.C. Allen, P.M. Tucker, R.A. Lewis, X-ray photoelectron spectroscopy study of the initial oxidation of uranium metal in oxygen + water-vapour mixtures, J. Chem. Soc. Faraday Trans. 80 (1984) 991–1000.
[75] G. Allen, P. Tucker, J. Tyler, Oxidation of uranium dioxide at 298 K studied by using X-ray photoelectron spectroscopy, J. Phys. Chem. 86 (1982) 224–228.
[76] G. Allen, P. Tucker, J. Tyler, The behaviour of uranium oxides in low partial pressures of O 2 studied using X-ray photoelectron spectroscopy, Vacuum 32 (1982) 481–486.
[77] G.C. Allen, P.A. Tempest, Linear ordering of oxygen clusters in hyperstoicheiometric uranium dioxide, J. Chem. Soc. Dalton Trans. (1982) 2169–2173.
[78] G. Allen, P. Tempest, Ordered defects in the oxides of uranium, Proc. R. Soc. Lond. A (1986) 325–344.
[79] G.C. Allen, J.C. Stevens, The behaviour of uranium metal in hydrogen atmospheres, J. Chem. Soc. 84 (1988) 165–174.
[80] V. Wheeler, The diffusion and solubility of hydrogen in uranium dioxide single crystals, J. Nucl. Mater. 40 (1971) 189–194.
[81] D. Sherman, D. Olander, Hydrogen dissolution in and release from nonmetals: I. Uranium dioxide, J. Nucl. Mater. 166 (1989) 307–320.
[82] J. Bloch, E. Swissa, M. Mintz, Heat-induced surface modifications affecting initial hydriding kinetics in uranium, Zeitschrift für Physikalische Chemie 164 (1989) 1193–1198.
[83] J. Bloch, M.H. Mintz, The effect of thermal annealing on the hydriding kinetics of uranium, J. Less Common Met. 166 (1990) 241–251.
[84] K. Gayer, W. Bos, The reaction of hydrogen with cerium metal at 25 °C, J. Phys. Chem. 68 (1964) 2569–2574.
[85] A. Efron, Y. Lifshitz, I. Lewkowicz, M. Mintz, Kinetics and mechanism of titanium hydride formation, Zeitschrift für Physikalische Chemie 164 (1989) 1255–1256.
[86] J. Petherbridge, J. Knowles, S. Bazley, The effect of thermal pre-treatments on the nucleation of uranium hydride, Solid State Ionics 292 (2016) 110–115.
[87] E. Swissa, N. Shamir, M.H. Mintz, J. Bloch, Heat-induced redistribution of surface oxide in uranium, J. Nucl. Mater. 173 (1990) 87–97.
[88] J. Knowles, I. Findlay, D. Geeson, S. Bazley, The influence of vacuum annealing on the nucleation and growth kinetics of uranium hydride, MRS Proceedings, Cambridge Univ. Press, 2012 (pp. mrss12-1444-y1410-1410).
[89] J. Condon, Nucleation and growth in the hydriding reaction of uranium, J. Less Common Met. 73 (1980) 105–112.
[90] C.P. Jones, T.B. Scott, J.R. Petherbridge, J. Glascott, A surface science study of the initial stages of hydrogen corrosion on uranium metal and the role played by grain microstructure, Solid State Ionics 231 (2013) 81–86.
[91] J. Glascott, A model for the initiation of reaction sites during the uranium?hydrogen reaction assuming enhanced hydrogen transport through thin areas of surface oxide, Philos. Mag. 94 (2014) 221–241.
[92] M.A. Hill, R.K. Schulze, Aging Study of Uranium Hydride Formation, Los Alamos National Laboratory (LANL), 2011.
[93] M.A. Hill, R.K. Schulze, Aging Study of Hydrogen Reactivity on Uranium Surfaces, Los Alamos National Laboratory (LANL), 2011.
[94] A. Banos, C.P. Jones, T.B. Scott, The effect of work-hardening and thermal annealing on the early stages of the uranium-hydrogen corrosion reaction, Corros. Sci. (2018) 147–155.
[95] D. Moreno, R. Arkush, S. Zalkind, N. Shamir, Physical discontinuities in the surface microstructure of uranium alloys as preferred sites for hydrogen attack, J. Nucl. Mater. 230 (1996) 181–186.
[96] A. Banos, C.A. Stitt, T.B. Scott, The effect of sample preparation on uranium hydriding, Corros. Sci. 113 (2016) 91–103.
[97] N. Shamir, D. Schweke, A. Rubin, T. Livneh, S. Zalkind, Carbon-enhanced hydriding of oxidized U-0.1 wt% Cr surfaces, IOP Conference Series: Materials Science and Engineering, IOP Publishing, 2010, pp. 012–037.
[98] N. Harker, T. Scott, C. Jones, J. Petherbridge, J. Glascott, Altering the hydriding behaviour of uranium metal by induced oxide penetration around carbo-nitride inclusions, Solid State Ionics 241 (2013) 46–52.
[99] J. Bingert, R. Hanrahan, R. Field, P. Dickerson, Microtextural investigation of hydrided α-uranium, J. Alloys Compd. 365 (2004) 138–148.
[100] R.J. Hanrahan, M.E. Hawley, G.W. Brown, The influence of surface morphology and oxide microstructure on the nucleation and growth of uranium hydride on alpha uranium, MRS Proceedings, Cambridge Univ. Press, 1998, p. 43.
[101] A. Banos, T.B. Scott, Statistical analysis of UH_3 initiation using electron backscattered diffraction (EBSD), Solid State Ionics 296 (2016) 137–145.
[102] A. Banos, Investigation of Uranium Corrosion Under Mixed Water-hydrogen

Environments, PhD Thesis, School of Physics, University of Bristol, 2017.
[103] J. Bloch, M.H. Mintz, The hydriding kinetics of β-quenched uranium-0.1 wt.% chromium, J. Alloys Compd. 241 (1996) 224–231.
[104] R. Rundle, The structure of uranium hydride and deuteride, J. Am. Chem. Soc. 69 (1947) 1719–1723.
[105] A. Bulbich, Effect of dissolved hydrogen on the ductile properties of metals as a result of nucleation on dislocations, J. Alloys Compd. 196 (1993) 29–36.
[106] T. Totemeier, R. Pahl, S. Hayes, S. Frank, Characterization of corroded metallic uranium fuel plates, J. Nucl. Mater. 256 (1998) 87–95.
[107] K. Balasubramanian, W.J. Siekhaus, W. McLean, Potential energy surfaces for the uranium hydriding reaction, J. Chem. Phys. 119 (2003) 5889–5900.
[108] J. Bloch, The kinetics of a moving metal hydride layer, J. Alloys Compd. 312 (2000) 135–153.
[109] J. Condon, Alternative model for nonstoichiometry in uranium hydride, J. Phys. Chem. 79 (1975) 42–48.
[110] J. Kirkpatrick, J. Condon, The linear solution for hydriding of uranium, J. Less Common Met. 172 (1991) 124–135.
[111] G. Powell, R. Ceo, W. Harper, J. Kirkpatrick, The kinetics of the hydriding of uranium metal II, Zeitschrift für Physikalische Chemie 181 (1993) 275–282.
[112] J. Tanski, R. Hanrahan, M. Hawley, Model for the Initiation and Growth of Metal Hydride Corrosion, Los Alamos National Laboratory, New Mexico, USA, 2000.
[113] A. DeMint, J. Leckey, Effect of silicon impurities and heat treatment on uranium hydriding rates, J. Nucl. Mater. 281 (2000) 208–212.
[114] J. Stakebake, Kinetics for the reaction of hydrogen with uranium powder, J. Electrochem. Soc. 126 (1979) 1596–1601.
[115] C.D. Taylor, R.S. Lillard, Ab-initio calculations of the hydrogen–uranium system: surface phenomena, absorption, transport and trapping, Acta Mater. 57 (2009) 4707–4715.
[116] C. Stitt, C. Paraskevoulakos, N. Harker, A. Banos, K. Hallam, C. Jones, T. Scott, Real-time, in-situ deuteriding of uranium encapsulated in grout; effects of temperature on the uranium-deuterium reaction, Corros. Sci. 127 (2017) 270–279.
[117] A. Sunwoo, D. Goto, Effects of processing on microstructure and properties of α-uranium formed parts, Scr. Mater. 47 (2002) 261–266.
[118] W. Siekhaus, P. Weber, I. Hutcheon, J. Matzel, W. McLean, Hydrogen accumulation in and at the perimeter of U–C–N–O inclusions in uranium – a SIMS analysis, J. Alloys Compd. 645 (2015) S225–S229.
[119] W. Davies, Report KAPL, Knolls Atomic Power Laboratory (USA), 1965.
[120] H. Inouye, A. Schaffhauser, Low-temperature Ductility and Hydrogen Embrittlement of Uranium – A Literature Review, Oak Ridge National Laboratory, Tennessee, USA, 1969.
[121] H.R.J. Gardner, Trans. ASM, 1960.
[122] M.P. Adamson, S. Orman, G. Picton, The effects of hydrogen on the tensile properties of uranium when tested in different environments, J. Nucl. Mater. 33 (1969) 215–224.
[123] C. Beevers, G. Newman, Hydrogen embrittlement in uranium, J. Nucl. Mater. 23 (1967) 10–18.
[124] R. Musket, G. Robinson-Weis, R. Patterson, Modification of the Hydriding of Uranium Using Ion Implantation, MRS Proceedings, Cambridge Univ. Press, 1983, p. 753.
[125] R. Musket, G. Robinson-Weis, R. Patterson, Decreasing the Hydriding of Uranium Using Ion Implantation, Lawrence Livermore National Laboratory, CA (USA), 1983.
[126] R. Musket, Suppression of the uranium-hydrogen reaction using high-dose carbon implantation, MRS Proceedings, Cambridge Univ. Press, 1987, p. 49.
[127] A. Ayral, D. Crusset, G. Raboisson, Surface modification of uranium alloys by ion implantation and ion mixing-effects on corrosion behavior, MRS Proceedings, Cambridge Univ. Press, 1992, p. 395.
[128] D. Crusset, F. Bernard, E. Sciora, N. Gerard, Modification of the hydriding kinetics of U-0.2 wt.% V alloy using ion implantations, J. Alloys Compd. 204 (1994) 71–77.
[129] R. Arkush, M. Mintz, N. Shamir, Passivation of uranium towards air corrosion by N^{2+} and C^{+} ion implantation, J. Nucl. Mater. 281 (2000) 182–190.
[130] A. Nelson, T. Felter, K. Wu, C. Evans, J. Ferreira, W. Siekhaus, W. McLean, Uranium passivation by C^{+} implantation: a photoemission and secondary ion mass spectrometry study, Surf. Sci. 600 (2006) 1319–1325.
[131] D. Crusset, Modifications of the hydriding kinetics of a metallic surface using ion implantation, J. Alloys Compd. 204 (1–2) (1994) 71–77.
[132] M. Yoo, Slip modes of alpha uranium, J. Nucl. Mater. 26 (1968) 307–318.
[133] C. Calhoun, J. Wollmershauser, D. Brown, R. Mulay, E. Garlea, S. Agnew, Thermal residual strains in depleted α-U, Scr. Mater. 69 (2013) 566–569.
[134] C.P. Jones, T.B. Scott, J.R. Petherbridge, Structural deformation of metallic uranium surrounding hydride growth sites, Corros. Sci. 96 (2015) 144–151.
[135] A. Crocker, The crystallography of deformation twinning in alpha-uranium, J. Nucl. Mater. 16 (1965) 306–326.
[136] J. Cathcart, Gaseous Oxidation of U Alloys, Physical Metallurgy of Uranium Alloys, Metals and Ceramics, Information Center, Columbus, Ohio, 1976, pp. 775–813.
[137] C. Stitt, M. Hart, N. Harker, K. Hallam, J. MacFarlane, A. Banos, C. Paraskevoulakos, E. Butcher, C. Padovani, T. Scott, Nuclear waste viewed in a new light; a synchrotron study of uranium encapsulated in grout, J. Hazard. Mater. 285 (2015) 221–227.
[138] C.D. Taylor, T. Lookman, R.S. Lillard, Ab initio calculations of the uranium–hydrogen system: thermodynamics, hydrogen saturation of α-U and phase-transformation to UH_3, Acta Mater. 58 (2010) 1045–1055.
[139] C. Stitt, C. Paraskevoulakos, N. Harker, C. Jones, T. Scott, The effects of metal surface geometry on the formation of uranium hydride, Corros. Sci. 98 (2015) 63–71.
[140] R. Lillard, C. Taylor, J. Wermer, N. Mara, J. Cooley, A thermal desorption study of the kinetics of uranium hydride decomposition, J. Nucl. Mater. 444 (2014) 49–55.
[141] A. Danon, J. Koresh, M. Mintz, Temperature programmed desorption characterization of oxidized uranium surfaces: relation to some gas-uranium reactions, Langmuir 15 (1999) 5913–5920.
[142] H. Idriss, Surface reactions of uranium oxide powder, thin films and single crystals, Surf. Sci. Rep. 65 (2010) 67–109.
[143] T. Kondo, E. Verink, F. Beck, M. Fontana, Gas chromatographic and gravimetric studies of uranium oxidation mechanism, Corrosion 20 (1964) 314t–320t.
[144] T. Kondo, F. Beck, M. Fontana, A gas chromatographic study on the kinetics of uranium oxidation in moist environments, Corrosion 30 (1974) 330–341.
[145] C. Colmenares, Oxidation mechanisms and catalytic properties of the actinides, Prog. Solid State Chem. 15 (1984) 257–364.
[146] K. Winer, C. Colmenares, R. Smith, F. Wooten, Interaction of water vapor with clean and oxygen-covered uranium surfaces, Surf. Sci. 183 (1987) 67–99.
[147] B. Hopkinson, Kinetics of the uranium-steam reaction, J. Electrochem. Soc. 106 (1959) 102–106.
[148] J. Waber, A Review of the Corrosion Behavior of Uranium, Los Alamos Scientific Laboratory, New Mexico (USA), 1956.
[149] T. Martin, C. Coe, P. Bagot, P. Morrall, G.W. Smith, T. Scott, M. Moody, Atomic-scale studies of uranium oxidation and corrosion by water vapour, Sci. Rep. 6 (2016).
[150] D.H. Wood, S.A. Snowden, H.J. Howe, L.L. Thomas, D.W. Moon, H.R. Gregg, P.E. Miller, Regarding the chemistry of metallic uranium stored in steel drums, J. Nucl. Mater. 209 (1994) 113–115.
[151] S. Zalkind, R. Eshkenazy, S. Harush, D. Halperin, D. Moreno, E. Abramov, A. Venkert, Stress corrosion cracking of U-0.1% Cr in humid helium atmosphere, J. Nucl. Mater. 209 (1994) 169–173.
[152] R. Orr, H. Godfrey, C. Broan, D. Goddard, G. Woodhouse, P. Durham, A. Diggle, J. Bradshaw, Formation and physical properties of uranium hydride under conditions relevant to metallic fuel and nuclear waste storage, J. Nucl. Mater. 477 (2016) 236–245.
[153] C. Stitt, N. Harker, K. Hallam, C. Paraskevoulakos, A. Banos, S. Rennie, J. Jowsey, T. Scott, An investigation on the persistence of uranium hydride during storage of simulant nuclear waste packages, PLoS One 10 (2015) e0132284.
[154] T.C. Totemeier, A Review of the Corrosion and Pyrophoricity Behavior of Uranium and Plutonium, Government Research Announcements and Index (USA), 1995, p. 45.
[155] G. Powell, Reaction of Oxygen with Uranium Hydride, Advanced Materials for Energy Conversion II, TMS (The Minerals, Metals, and Materials Society), Warrendale, PA, 2004, p. 206.
[156] T.C. Totemeier, S.L. Hayes, Analytical and numerical models of uranium ignition assisted by hydride formation, DOE Spent Nuclear Fuel and Fissile Material Management Conference (1996).
[157] A.D. Shugard, G.M. Buffleben, M.P. Kanouff, S.C. James, D.B. Robinson, B.E. Mills, P.E. Gharagozloo, P. Van Blarigan, Rapid Hydrogen Gas Generation Using Reactive Thermal Decomposition of Uranium Hydride, Report SAND2011-6939, Sandia National Laboratories, 2011.
[158] A. Ritchie, A review of the rates of reaction of uranium with oxygen and water vapour at temperatures up to 300 °C, J. Nucl. Mater. 102 (1981) 170–182.
[159] P. Morrall, D. Price, A. Nelson, W. Siekhaus, E. Nelson, K. Wu, M. Stratman, W. McLean, ToF-SIMS characterization of uranium hydride, Philos. Mag. Lett. 87 (2007) 541–547.
[160] C. Berthinier, S. Coullomb, C. Rado, E. Blanquet, R. Boichot, C. Chatillon, Experimental study of uranium carbide pyrophoricity, Powder Technol. 208 (2011) 312–317.